LHCb Collaboration

LHCb 2003-043 RICH
28th November, 2003

Performance of Multianode Photo Multiplier Tubes at Low Gain

S. Eisenhardt[1], **F. Muheim**
University of Edinburgh

Abstract

A study of the signal response of Multianode Photo Multiplier Tubes (MaPMT) is presented for gains spanning the range of at least $3 \cdot 10^4 < G < 5 \cdot 10^6\, e^-$. The feasibility of running the MaPMT at gains of around 30000 e^- is investigated to evaluate the direct readout of MaPMT with front-end chips that have been developed for silicon detector or micro strip gas chambers. In order to characterise the shape of the signal spectra and to specify the loss of signal below a threshold cut an improved fitting algorithm is used.

[1]Corresponding author. E-mail: S.Eisenhardt@ed.ac.uk

1 Introduction

Multianode Photomultiplier Tubes (MaPMT) have been accepted by the LHCb collaboration as backup technology for the RICH photodetectors [1, 2, 3]. In preparation of the proposal [4] the performance of the MaPMT as a photo detector was studied. The results from the tests carried out with light emitting diodes (LED) and beam particles as sources of photons are described in [5]. Earlier measurements can be found in [6, 7, 8, 9].

In order to keep the MaPMT option on a viable path towards a functional detector in time for the experiment the front-end electronics has to be optimised in parallel to the development on the baseline technology. In general ASIC front-end chips shall be used which already have been developed for the read-out of silicon detectors or Micro Strip Gas Chambers (MSGC). These detectors produce signals which are about an order of magnitute smaller than those from MaPMTs. There are three ways possible to adapt the dynamic ranges of the MaPMT signals and the ASIC input circuits: (1) by redesigning the input stage of a chosen front-end chip or (2) by attenuating the MaPMT signal between tube and ASIC or (3) by driving the MaPMT at a sufficiently low gain.

The first option has been tried by implementing test structures into the Beetle chip (submission BeetleMA_1.0) [10]. The results recently became available and look very promising but this option still needs a dedicated effort in R&D to finally become available as a readout option for the MaPMT.

The second option was used in the tests reported in [5]. The front-end ASIC chip used was the APVm running at a 40 MHz clock [11]. To attenuate the MaPMT signals an AC-coupler made of gold tracks laid on a ceramic base was used between the MaPMT and the APVm. As reported in [5] this approach suffered from cross-talk between neighbouring channels on the ceramic (15 %, symmetric) as well as from cross-talk within the APVm input circuit (1...33 %, asymmetric). Although the first source can be reduced principally by the introduction of an additional grounding plane under the ceramic such a solution is not favourable.

The object of this study is to understand the signal shape of the MaPMTs using the third option. It is updating and extending a preliminary study [12] which was limited in the noise level of the used CAMAC electronics and which used a relatively simple Gaussian algorithm to fit the signal spectra. Consequently it was lacking a proper estimate of the signal loss introduced by a threshold cut.

In this study the gain of the MaPMT again is studied as a function of the applied high voltage. And again an additional reduction of the gain is achieved by changing the ratios of the resistors of the bleeder chain which define the potentials between the dynodes of the MaPMT. But this time the APVm based readout described in [5] is used. It features the data acquisition at LHC speed and an improved noise level with respect to the CAMAC readout. In a second readout option the attenuation provided by the AC-coupler then is bypassed and the MaPMT signals generated at a very low gain of approximately 30000 e^- are fed directly into the APVm. As a reference to compare with a slightly improved CAMAC readout was used to obtain updated and extended results from new data as the old data from [12] was lost in a disk crash. The shape of the MaPMT signal spectra is characterised with an improved fitting algorithm which is based on the Poisson distribution and provides a significantly improved description of the shape of the signal spectra as discussed in [13]. Based on the improved understanding of the signal spectra the loss of photon signals below a threshold cut is derived from the fits to the measured data and the readout options are compared.

2 Multianode Photomultiplier Tubes

A sketch of the Multianode Photomultiplier Tubes (MaPMT) R7600-03-M64, manufactured by Hamamatsu, is shown in Figure 1. A tube consist of an array of square anodes each having its own 12-stage metal dynode chain to multiply photoelectrons, with all channels incorporated into a single vacuum tube. The "M64" configuration constitutes the densest pixelization available, 8×8 pixels with an anode size of $2.0 \times 2.0\,\mathrm{mm}^2$, with the anodes separated by 0.3 mm gaps. This provides the spatial resolution required for the LHCb RICH detectors. The "03" option refers to the 0.8 mm thick UV-glass window which features a threshold for light transmission at a wavelength of 200 nm. The photons are converted into photoelectrons in a semi-transparent Bialkali photocathode deposited on the inner side of the window. The mean gain of the MaPMT through its 12-stage dynode chain is about 3×10^5 when operated at a voltage of 800V.

Emerging from the photocathode the photoelectrons pass a focusing mask and a mask of entry windows on their way to the first dynodes (see Figure 3 for illustration). The focusing mask consists of $\sim 75\,\mu$m thin wires and is kept on the same potential as the photocathode. For each pixel there are two entry windows in front of the first dynode. They are shaped as rectangular slits of approximate size $\sim 1.8 \times 0.5\,\mathrm{mm}^2$ separated by a catwalk of ~ 0.5 mm. There is also a focusing wire spun above this catwalk making sure

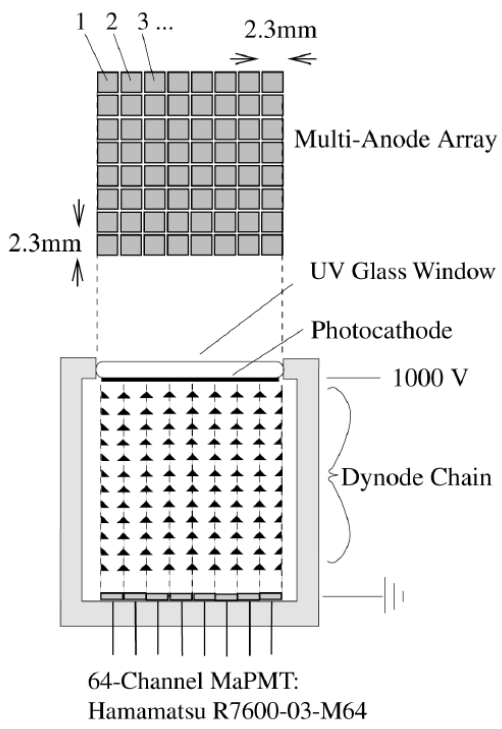

Figure 1: Sketch of the top and side view of a MaPMT.

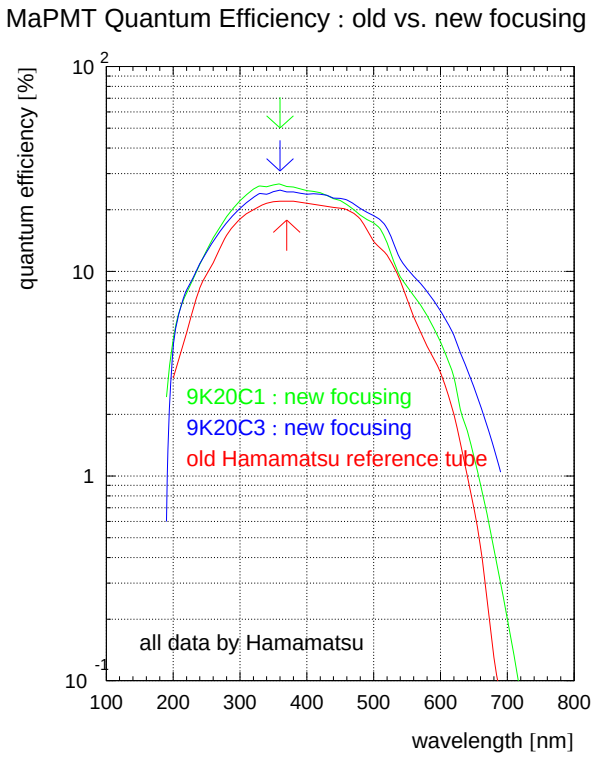

Figure 2: Quantum efficiency of the MaPMT R7600-03-M64 as a function of wavelength, measured by Hamamatsu.

Dynode	PC	1	2	3	4	5	6	7	8	9	10	11	12	Anode
Resistor	R_1	R_2	R_3	R_4	R_5	R_6	R_7	R_8	R_9	R_{10}	R_{11}	R_{12}	R_A	
high-gain (default)	3	2	2	1	1	1	1	1	1	1	1	2	5	
medium-gain	4	2	2	1	1	1	1	1	1	1	1	2	5	
low-gain	4	3	3	1	1	1	1	1	1	1	1	2	5	

Table 1: Resistances R in $[10^5\,\mathrm{k}\Omega]$ in front of each dynode. The default resistor chain proposed by Hamamatsu is the "high-gain" option.

that the photoelectron collection efficiency in this centre region of the pixel is better than 80 % of the maximum efficiency of the pixel (shown by the scans across the pixel MaPMT surface which were presented in [5, 12]). The effective pixel size defined by the 50 % efficiency point was measured to 2.1 mm at the UV-glass window [5], a little larger than the 2.0 mm reported by the manufacturer.

For the tests described in [5] nine MaPMTs have been purchased, preselected such that the average gain of the tubes varies not more than a factor of two. Afterwards Hamamatsu has improved the quantum efficiency and the focusing properties of the MaPMT. Two further tubes with the improved ("new") specs were acquired.

The quantum efficiency of the MaPMT, measured by Hamamatsu, is plotted versus the wavelength of the photons in Figure 2. Whereas the quantum efficiency of the old series has a maximum of 22 % at 380 nm the new tubes have a maximum of 27 % and 25 % at 360 nm, respectively. This improvement was achieved by a change in the production process [14]. An improvement in the focusing [5, 12] of the photoelectrons onto the entry slits was achieved by altering the focusing mask as depicted in Figure 3. The new mask allows for a wider entry area at the edges of the acceptance where also additional focusing wires are placed. In addition the distance between the focusing mask and the entry slits has been reduced.

To study the tubes at reduced gain the ratio of the resistors in the dynode chain has been varied. For a Poissonian distribution of secondary electrons emerging from a dynode on the impact of one electron the relative width of the resulting spectrum is $\sigma_1/Q_1 = \sqrt{N}/N$, with Q_1 and σ_1 the measured gain and

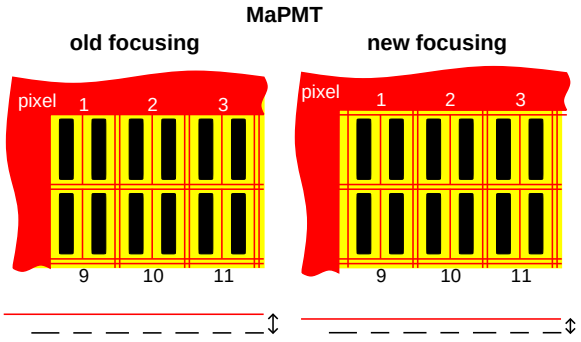

Figure 3: The mask of focusing wires (dark grey) and the mask of entry windows (light grey) in front of the dynode chains (black) for the old and the new focusing scheme. Also indicated is the distance of the focusing grid and the mask of entry windows.

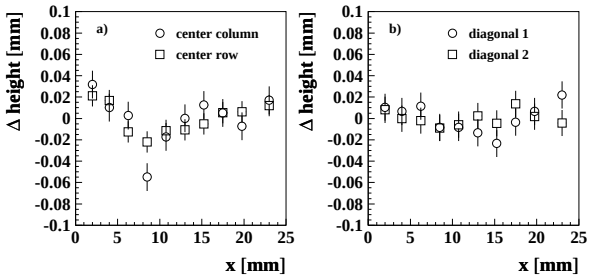

Figure 4: Height differences in the window plane of MaPMT 9C20A2: a) vertical and horizontal scan in the middle of the tube, b) scan along the two diagonals.

width of the single photon signal and N the average multiplication factor at this dynode. Therefore the relative width of the single photoelectron spectrum at the anode is dominated by the relative width of the distribution generated at the first dynode. The main idea now is to keep the electron multiplication at a given supply voltage large for the first or first few dynodes while reducing the multiplication in the subsequent stages. The product sum over the dynode stages then results in a lower total gain while the signal broadening in the statistical multiplication process is maintained. In Table 1 the resistor values are given for the three sets of resistor chains which were used to distribute the supply voltage to the dynodes. The three sets differ only in the values R for the resistors in front of the first three dynodes. The default resistor chain proposed by Hamamatsu is the "high-gain" option. This option is used unless stated otherwise.

2.1 Window Surface Flatness

One of the customisations of the MaPMT R7600-03-M64 for the use in LHCb is the UV-glass window which extends the spectral sensitivity down to about 200 nm. While production this 0.8 mm thick window is melted into a pre-produced glass tube to form the glass envelope of the final MaPMT. The window surface needs to be optically coupled to lenses in the RICH detectors of the LHCb experiment.

To understand the quality of the MaPMT window scans across the surface have been taken using a spherometer with a display accuracy of ± 0.005 mm. A plane surface was placed at the approximate height of the MaPMT window fixed with respect to the MaPMT position. The tripod of the spherometer was positioned on this plane measuring the relative height of selected locations on top of the window with respect to the plane. The point of the spherometer was screwed from the top towards the window surface and the position taken at which one of the tripod feet lifted from the supporting plane. Thus, a relative accuracy of ± 0.02 mm was achieved. The surface of the tube was scanned vertically, along the tube columns, horizontally, along the rows, as well as along both diagonals always through the centre of the tube. The step size of the point grid on top of the window surface varied between 2.0 mm and 2.5 mm with a relative error of ± 0.5 mm to each point.

Each scan individually was fitted with a linear function. The deviations to the linear fits are plotted in Figure 4. One can see that the maximum amplitude in the unevenness of the window is below 0.1 mm. In fact, this maximum value is due to a specific distortion of the investigated window not present, at least to that extend, in the windows of the other available tubes. Beside of this distortion the window rather seems to be even within ± 0.03 mm, i.e. not much larger than the accuracy of the measurement.

To learn how parallel the window is positioned with respect to the base plate of the MaPMT the total height of the MaPMT housing was measured with a vernier calliper at the four corners. In our sample of tubes generally 19.9 ± 0.1 mm was found; only for the tube presented in Figure 4 (9C20A2) three corners were measured to 20.1 ± 0.1 mm and one corner to 20.5 mm, i.e. still within the tolerance quoted by Hamamatsu: 20.1 ± 0.5 mm.

Therefore the situation presented in Figure 4 can be assumed as a worst case scenario.

3 Readout Channel Capacities

The noise level present in the channels of a front-end chips like the Beetle or the APVm consists of a constant part and one depending on the total capacity in front of the chip input. For the Beetle a noise level of $ENC \approx 450\,e^- + 47\,e^-/pF$ is achieved [10]. In order to finally achieve a total noise level of about $ENC \approx 1000\,e^-$ the total capacity of the readout channel in front of the chip should not exceed a capacity of 10 pF.

To determine the contribution to the channel capacity by the various components used so far a series of measurements has been done for one MaPMT (9C24C1), a single base, the Hamamatsu bleeder board as the base of 4×4 MaPMTs and the Kapton cables used in the APVm setup.

The capacities were measured using a capacity meter with a 10kHz switching circuit[2] with a relative device accuracy of about ± 0.005 pF. The absolute calibration of the unit was cross-checked with polystyrene capacities in the range $1 \ldots 10$ pF which were measured to within 5 % of their nominal value. Thin leads were used to connect the contacts of the tested device to the capacity meter. The uncertainty introduced by (re-)placing the contacts to the pins causing the wire paths to be slightly different was tested to be ± 0.05 pF. Thus, the total reproducibility for each measurement point was assumed as ± 0.055 pF.

In order to take into account the effect of the capacity produced by the distance of the connecting leads it was measured for a range of distances without a test object connected. The resulting capacity in the range from 0.2 pF to 0.5 pF was then parameterised according to the specific geometry of a data set and then subtracted from the measured data.

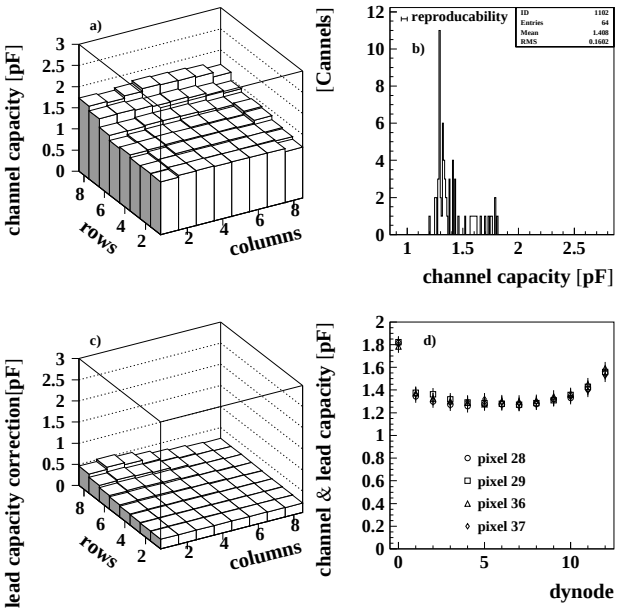

Figure 5: Channel capacities of the MaPMT 9C24C1: a) & b) capacities of the MaPMT channels measured against the photo cathode and corrected for lead capacities, c) parameterised correction for lead capacities, d) capacities as measured of the four centre MaPMT channels against all dynodes and the photo cathode (dynode 0).

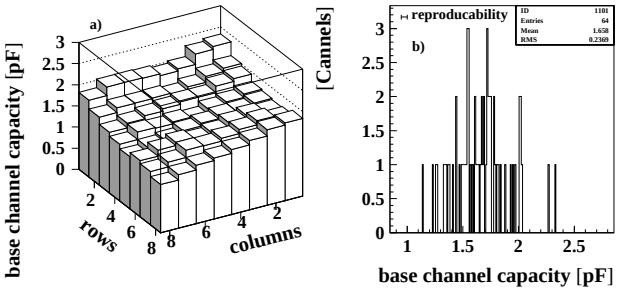

Figure 6: Channel capacities of a single base for a MaPMT, corrected for lead capacities.

Figure 5c shows the parameterised correction for the measurement of the MaPMT channel capacity against the photo cathode. The peak position lies next to the photo cathode pin. Figures 5a and 5b present the resulting corrected channel capacities of the MaPMT tube. Still the relative position of the channel to the second connection influences the measured capacity of the channel to an extend which is of the same order as the lead capacities. This is believed to be due to the internal geometry of the MaPMT. A corresponding behaviour was found when the channel capacities were measured against the dynode 6 and the dynode 12 whose pins are positioned at different sides of the tube. In Figure 5d the capacities of the four centre pixels of the MaPMT are plotted as they were measured against all dynodes and the photo cathode – the latter displayed as dynode 0. As the connecting pins to the dynodes are arranged as a ring around the pin grid array of the pixels the distances of all dynode pins to the centre pixels are similar. The results for the four centre pixels are virtually the same. The largest capacity is measured against the photo cathode, presumably due to its large surface. For the dynodes close to the anodes the measured capacity is increased as well, consistent with the decrease of the distance. As there is no other ground within a MaPMT than the anodes themselves the capacity determined against the photo cathode is given as an upper limit of what a tube contributes to the total capacity of a readout channel in front of the readout chip: the average MaPMT channel capacity is 1.4 pF with a RMS of 0.16 pF.

Figure 6 presents the result for the corresponding measurement for a single base manufactured by Hamamatsu. The varying capacity component due to the base geometry is about twice as large than for

[2] Wayne Kerr Automatic LCR Meter 4210.

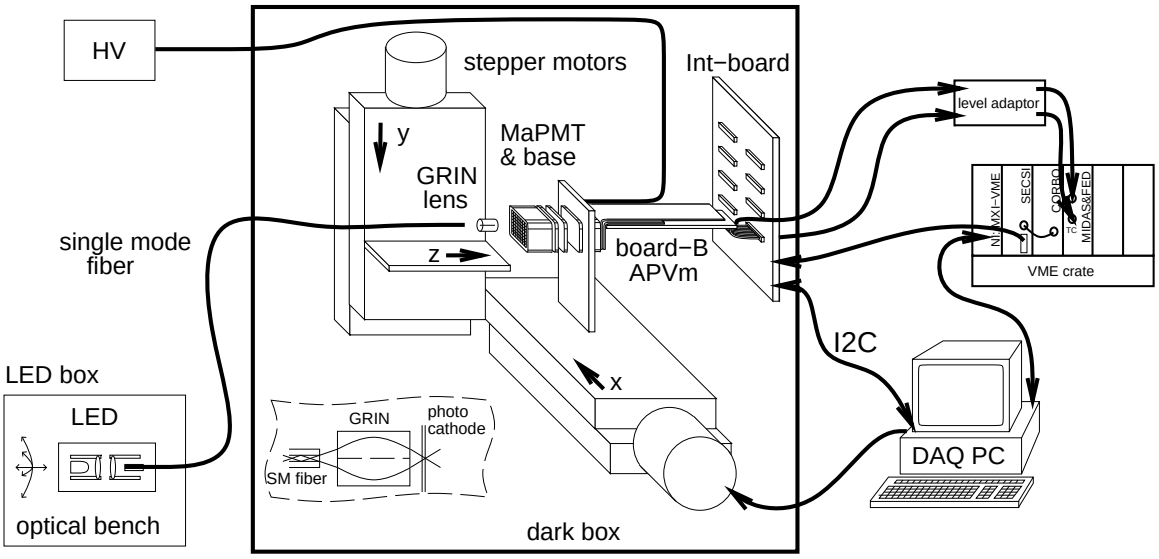

Figure 7: The MaPMT scanning facility using the APVm readout.

the MaPMT. The average channel capacity of a single base is 1.7 pF with a RMS of 0.24 pF.

A less thorough investigation of the Hamamatsu bleeder board, a prototype of a common base for 4×4 MaPMTs, showed that it has an average channel capacity of about 4.5 pF per channel.

The Kapton cables used to connect the MaPMT bases to the APVm readout boards in this study and in [5] were measured to have channel capacities between 14 pF and 33 pF in agreement with the values quoted in [5]. The bulk of this capacity actually is generated in the region of the pin grid array connecting to the MaPMT base where the four double layers of tracks and ground planes apparently get very close together. This is suggested by the fact that the channel capacities increase row-wise linear with the distance to the side where the cables are guided out. The capacity contributed by the free cable between the pin grid array and the connectors to the front-end board can be estimated from geometry to be about 2.4 pF and 4.8 pF for the short and the long arm, with average lengths of 60 mm and 120 mm, respectively.

Therefore great care is needed in the final design of the front-end board for a modul of 4×4 MaPMTs. It not only has to provide the mechanical stability, the voltage divider chain, the high voltage distribution, the front-end electronics, the connecting traces and the interfaces. But it also has to be designed with suitable measures to keep the channel capacities low at every stage to finally meet the aim of a total capacity of 10 pF per channel.

4 Data Acquisition Setup

4.1 Opto-mechanical Setup

The laboratory setup to measure the response of the MaPMTs to single photons using the APVm based readout is shown in Figure 7. The optical and mechanical part of the setup remains unaltered with respect to the setup using the CAMAC readout presented in [12] but is described more accurately here.

Light from a pulsed LED source with a wavelength of 470 ± 20 nm was coupled into a single-mode fibre and transmitted into the measurement box. The grounded measurement box also acted as a shield against external electronic noise. In front of the MaPMT surface the light from the single-mode fibre was focused by a gradient index lens (GRIN) (numerical aperture: N.A. $= 0.25$) via small air gaps. The focus with a diameter of about 100 μm or less was positioned at the location of the photocathode on the inside of the window of the MaPMT taking into account the refraction at the MaPMT window. The bias voltage driving the LED and defining the amount of light produced was set such that for about $20 - 30$ % of the events a photoelectron was produced at the photocathode within the timing gate.

The optical system was mounted on a vertically movable stage. The MaPMTs and the front-end electronics were mounted on a horizontally movable stage. The stages were moved by computer controlled stepper motors and had an accuracy and reproducibility of better than 10 μm over a travel range of

150 mm. Thus, an array of 4 × 4 MaPMTs, as proposed as the basic photodetector module of MaPMTs in [4], could be scanned over in an arbitrarily programmed way.

4.2 Readout Electronics and Front-end Setup

CAMAC Readout: For the data retaken with the CAMAC readout a similar but slightly improved setup was used compared to [12]. The signals from the tube were amplified by a factor of ×100 in two consecutive steps of ×10 by linear fast amplifiers (PS: 776 & LeCroy: 612 & 612A). The individual noise behaviour of the linear amplifier channels was quite different. In general the amplifier channels with the lower noise were used for the first amplification stage. In addition the better amplification channels of the first stage were matched to the better channels of the second stage giving two channels with the overall smallest electronic noise. The linear amplifiers also generated a DC offset of the order of a few mV which could be adjusted by screws only in a rather coarse way. To effectively suppress this DC component 1 pF decoupling capacities were soldered into the LEMO signal lines before the ADC input. The data was digitised by a 10-bit charge integrating ADC (LeCroy: 2249A) and read out by a PC via PCI-VME (NI: VME-PCI 8015) and VME-CAMAC (CES: CBD 8210 and CES: A2 2111) interfaces. The integration gate of the ADC was set to 200 ns. This system was capable to take data up to a constant trigger rate of 15 kHz and usually was operated at 10 kHz.

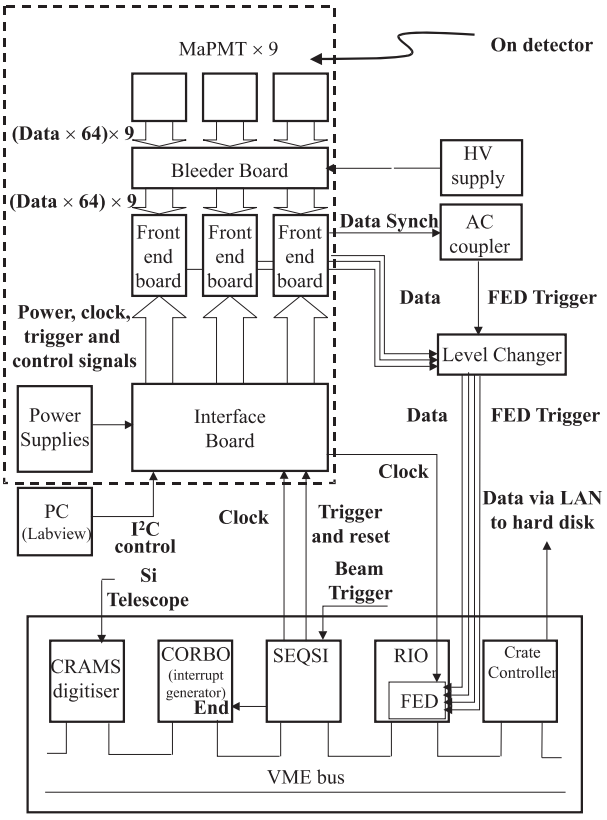

Figure 8: A schematic of the APVm based electronic readout and data acquisition system. Reproduced from [5]. The components in the dashed box, but not the power supplies, were located in the dark box as depicted in Figure 7.

CAMAC Front-End: Due to the limited amount of amplifier channels only 8 MaPMT channels could be read out at the same time. These channels were terminated by the 50 Ω input impedance of the subsequent electronics. The remaining anodes were terminated to ground via 9-pin 50 Ω termination bridges at the readout pins of the single base. This prevented a floating up of these anodes by the collection of charge from photon signals. The signals from the anode pins in this very narrow environment were picked up by 50 Ω coaxial cable of thin diameter (1.2 mm, RS: 388-530). The length of this cable was only 2 m limiting the signal distortion caused by this cable type to an acceptable level. The signal lines were interfaced to standard LEMO cables at the patch panel of the measurement box.

APVm Readout: The APVm based front-end electronics and data acquisition system used in this study was very similar to the readout electronics described for the 3 × 3 array of MaPMTs in [5]. Once set up the APVm, running at an external 40 MHz clock, sampled the 128 analogue signals every 25 ns and stored them into a 160-cells pipeline which was used as a circular buffer. Upon an external trigger one pipeline cell, a defined latency behind the actual writing position, was marked for read-out and later multiplexed to the analog output. A sketch of the data acquisition system is reproduced in Figure 8 to which only the differences are discussed in the following.

Due to the laboratory environment there was no SI beam telescope. Thus, the CRAMS digitiser to measure its signal simply could be omitted. There also was no beam trigger. Instead the signal to trigger an event to be read out was generated from the trigger pulse initiating the pulse generation to drive the LED. The timing of this trigger was determined by maximising the signal output while varying the latency of the APVm ASIC in steps of 25 ns. No I^2C bus extender card was used since the cable lengths were sufficiently short.

A different approach was used for the hardware of the data acquisitions system. At the test beam a VME based motherboard and processor unit (CES: 8061 RIO) was used which also carried the Front-End Digitiser (FED) [15, 16] in its PCI Mezzanine Card (PMC) interface. Instead, in the laboratory a PCI-VME interface (NI: VME-PCI 8015) was used to memory-map the used VME address space onto the PCI

bus of a data acquisition PC as indicated in Figure 7. A VME-PMC interface (ACAL: Midas-20) was used to plug the FED into the DAQ system. Since the Midas-20 card used was an earlier version (C.1) it didn't yet provide the 3.3 V supply needed by the FED. Therefore this voltage was supplied externally via flying leads soldered to the capacity C 231 next to the Xilinx chip on the FED [16]. Finally, the used SEQSI module needed the provision of an extra -5.2V supply which was patched at the VME backplane to the pins C4 and C19 of the J2 connector.

The data acquisition program (C++) was altered to reflect the hardware alterations made and recompiled for the Windows NT operating system running on the DAQ PC. All these changes in the data acquisition system did not affect the signal read out from the MaPMTs. This system was capable to take data up to a constant trigger rate of 1.7 kHz and usually was operated at 1 kHz.

APVm Front-End: In order to be able to change the ratios of the resistors single bases instead of a bleeder board were used, each carrying its own voltage divider chain. Thus, the resistor chain for a single MaPMT was altered by swapping the individual single base. Due to the size of the single bases the pitch of MaPMT in this setup was 27.5 mm opposed to 26.5 mm on the bleeder board. The single bases were mounted to a frame on the side of the readout. It gave the array the mechanical support while for each base suitable cut-outs were provided for the individual ground and high voltage pins as well as for the array of signal pins. The Kapton cables were plugged on via additional pin-grid-arrays. The pin-grid-arrays were needed to make room for the distribution of the high voltage and ground potential from the HV power supply to the pins of the individual bases by the means of daisy-chained isolated cables. They also were needed as interface to fan out the ground potential of the photodetectors to the connected front-end boards. In order to avoid ground loops the routing of the ground was star-like shaped throughout the data acquisition electronics with the common point between the MaPMT bases and the front-end boards.

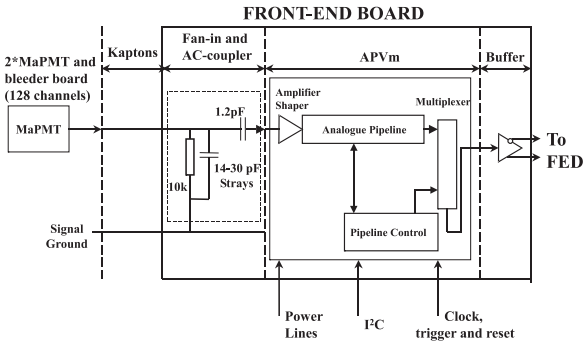

Figure 9: A schematic of the front-end board which carries the APVm ASIC and the ceramic with the AC-coupler network. Reproduced from [5].

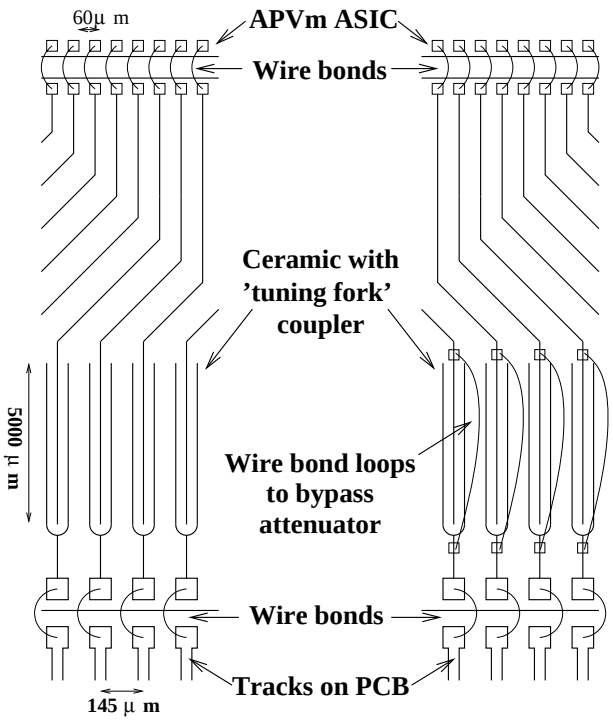

Figure 10: Two sections through the AC-coupler network. On the left with the standard layout and on the right the altered layout to bypass the 1.2 pF capacity used in the attenuation circuit.

For the standard way of readout the front-end board was used in the way documented in [5]. It carries the APVm ASIC and the AC-coupler network to achieve the needed attenuation by an approximate factor of $\div 10 \ldots 30$. A schematic layout of this board is reproduced in Figure 9. In order to test the operation of the MaPMTs at such a low gain that the signals could be fed into the APVm directly the attenuation network needed to be disabled. As depicted in Figure 9 the attenuation was achieved by a RC-element consisting of a parallel 1 kΩ resistor and a serial capacity of 1.2 pF. The capacity was made from gold tracks forming a 5 mm long fork on the AC-coupler ceramic as shown on the left side of Figure 10. To disable the attenuation network for a particular input channel the 1 kΩ resistor was removed from the front-end board and the capacity was bypassed by a long wire bond as indicated on the right side of Figure 10. Wire bonding over such a large distance ($> 5000\,\mu$m) stretched the used technology to the limit (automatic wedge bonding; 25 μm-Al wire; bonding on $\sim 40 \times 40\,\mu$m^2 pads which already existed on the tracks) but these changes to the front-end board were reversible and maintained the fan-in functionality of the AC-coupler ceramic. Extreme care had to be taken to avoid touching of

Parameter	Setting	Value
Latency	8	0.200 μs
Mode	peak	1-sample
Calibration	off	
IPRE: Preamp Bias	95	380 μA
ISHA: Shaper Bias	105	105 μA
IPSP: APSP Bias	75	38 μA
ISFB: Source Follower Bias	40	40 μA
VPRE: Preamp Control	145	-0.61 V
VSHA: Shaper Control	80	0.56 V
VADJ: Output Analog Offset	165	-1.48 V
VCAS: Cascode Bias	0	0.0 V
VCMP: Reference	255	-2.59 V
IREF: Reference	0	0.0 μA

Table 2: Operation parameters of the APVm on the front-end board with the attenuation disabled for 64 of its channels.

neighbouring wire bonds. One half side of one front-end board, corresponding to the 64 channels of one MaPMT, was altered in this way disabling the attenuation network. Thus, while reading out one MaPMT in the 'no attenuation' configuration the functionality of this board could still be cross-checked by reading out a second MaPMT in the 'standard configuration' using the other half of the front-end board. This proved to be a valuable feature while searching for a usable parameter space for the 'no attenuation' configuration.

In a comprehensive scan of the operation parameters for the APVm [17] it was confirmed that the optimal setting actually was identical for both configuration options of the front-end board. The optimal parameter setting of the APVm was defined with the overall goal to make the most use of the dynamic range of the APVm while maintaining a good signal quality. This included a small common mode and a small base line offset between the two set of channels from the two MaPMT inputs. The chosen parameter values for the front-end board with the 'no attenuation' configuration are listed in Table 2. The output analog offset (VADJ) had to be carefully tuned for each APVm chip individually, all other parameters were universal for the front-end boards used.

Using these parameters the APVm chips usually produced their data frames in the $0 \ldots 150\,\mathrm{mV}$ range as shown in trace (1) of Figure 11. In order to project this signal to the $0 \ldots +1.5\,\mathrm{V}$ input range of the 8-bit ADCs of the FED the signals were amplified and slightly level shifted on a level adaptor board located next to the FED as indicated in Figure 8.

4.3 Experimental Difficulties

In the course of working with the setup and its variations described above a couple of hardware flaws and failures were observed which required special treatment in the data acquisition procedure, correction of the raw data or even affect the final data quality.

Common Issues: When the stepper motors were powered the electromagnetic noise was so intense that it completely drowned the MaPMT signals and no shielding was sufficient. Only powering off the frame carrying the stepper motor controller and driver units while taking data ensured a noise free environment at the front-end. An interface to control the power state of stepper motor system was developed and integrated into the CAMAC data acquisition system.

The pulse generating circuit driving the LED, situated in the vicinity of the setup, also generated electromagnetic noise but the grounded measurement box provided sufficient shielding for the front-end setup.

CAMAC System: For the CAMAC system the most frequent problem was the breaking of signal or ground lines at the pick-up point behind the MaPMT base where space was very limited, the connections were frail and the cables had to be handled often. After fixing such problems the affected data had to be retaken.

As the used ADC developed a fault and the time to take the data was limited two series of the intended measurements for comparison with the corresponding APVm data are not available for this study.

APVm System: For the APVm based system the most complicated problem was the proper setup

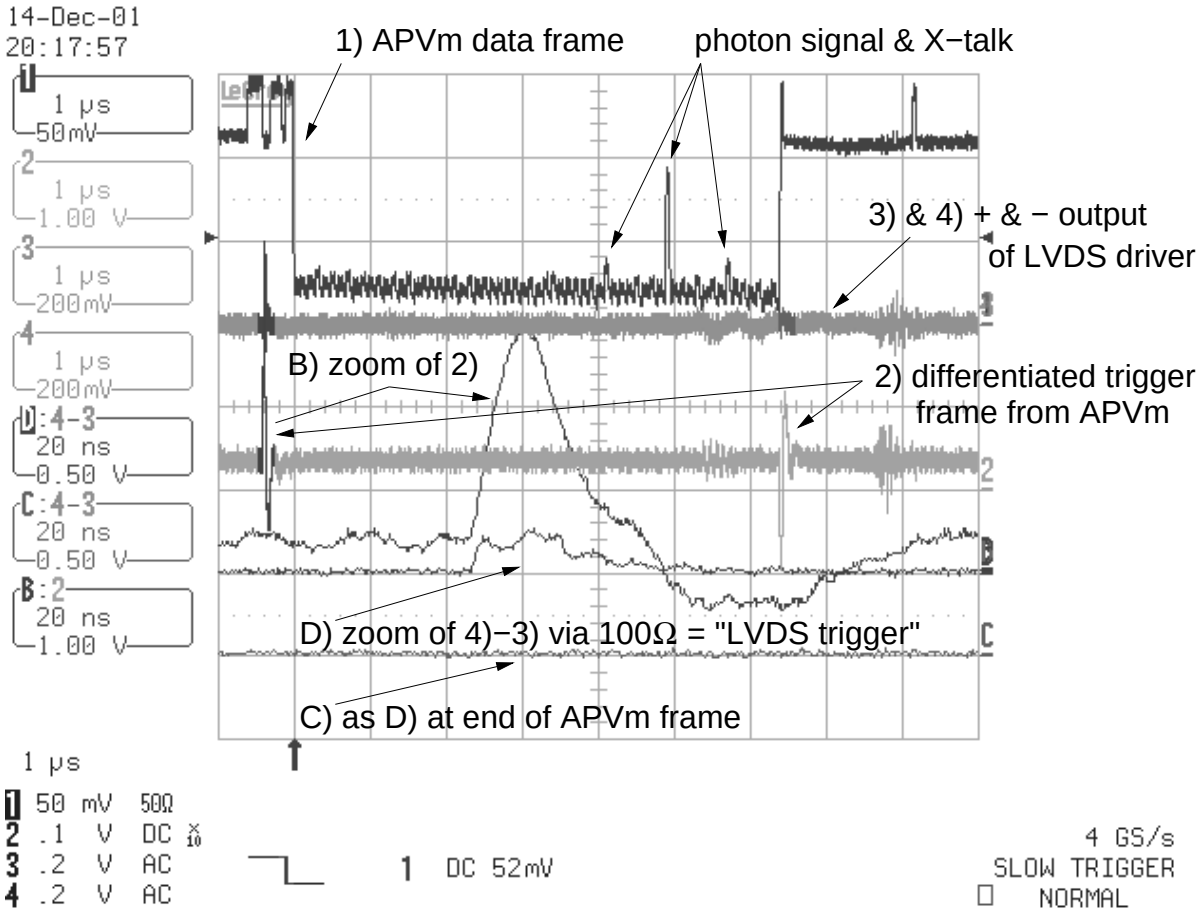

Figure 11: Screen shot of the LVDS trigger setup synchronising the APVm data frame with the FED.

of the trigger signal synchronising the APVm data frame with the digitising process in the FED. The relevant signals and their timing is documented in an oscilloscope screen shot in Figure 11.

Trace (1) shows at 1 μs/div the data frame sent out by the APVm chip cycled at half the data-sampling rate (20 MHz). Twelve header bits, four status bits and eight decoding the pipeline address, precede the 128 analogue data samples. There is a MaPMT signal visible in one channel and the cross-talk signals induced in the neighbouring channels of the AC-coupler network. The structure of the base line of the data was produced by the two groups of 64 channels associated with the two MaPMT tubes. They are interleaved in groups of two channels and sent out by the APVm at two base line levels with a small DC-offset.

Synchronous to the data output the APVm sent a trigger signal which changed level before the 5^{th} header bit and after the 128^{th} data bit. Using a 150 pF capacity less than 5 cm before the level adaptor board, cf. Figure 8, this signal was differentiated before it was amplified and converted into a LVDS type trigger signal and passed on to the trigger input of the FED. The input signal to the LVDS converter was picked up by a probe and is displayed as trace (2) showing the two pulses of the differentiated signal. A 20 ns/div zoom of the first pulse of this signal is shown in trace (B). The LVDS converter generates a trigger pulse for the time the input signal is larger than ~ 1.6 V - in the display approximately at the location of the base line of trace (2). The LVDS signal was made visible on the display by feeding the two LVDS output signals into channel (3) and (4) of the oscilloscope via a 100 Ω termination near the oscilloscope and displaying the difference in trace (D). It shows a typical result for an acceptable LVDS trigger pulse. The phase relation between the LVDS trigger and the APVm data frame at the FED was adjusted by cable delay in the data lines.

For proper operation of the data acquisition the width of the LVDS trigger pulse needed to fulfil the condition $\sim 15\,\text{ns} < \tau < 25\,\text{ns}$ while at the same time there may not be generated a LVDS trigger pulse from the second pulse on trace (2) at the end of the data frame. The absence of such a second trigger is documented in trace (C). The amplification and offset of the differentiated trigger signal, traces (2) and (B), had to be tuned accordingly and the window to meet the above conditions was small. There was no adjustment were all conditions could be met reliably over a long time.

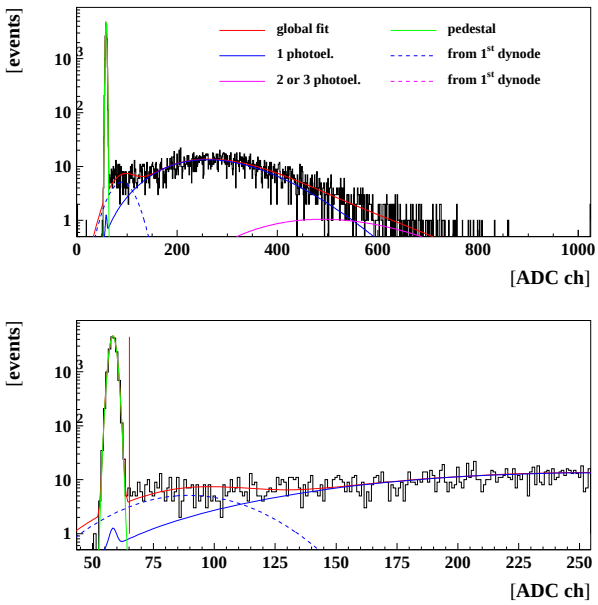

Figure 12: Typical good fit of a MaPMT signal spectrum form CAMAC data ("high-gain" resistor chain, tube 9C20A2, pixel 10, HV = -960 V); a zoom around the pedestal region is shown in the bottom plot; predominantly the signal from single photo electrons is visible.

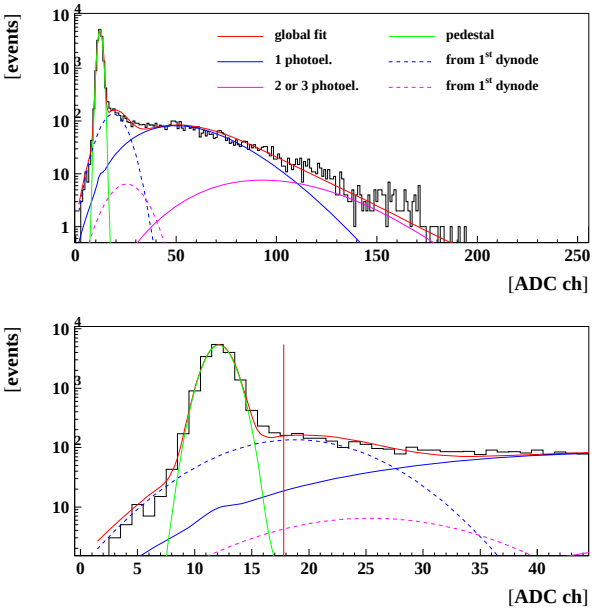

Figure 13: Typical good fit of a MaPMT signal spectrum form APVm data ("high-gain" resistor chain, 'standard configuration' front-end board, tube 9C20A2, pixel 10, HV = -940 V); a zoom around the pedestal region is shown in the bottom plot.

Instead, an adjustment was chosen where no or only very few triggers were missed due to an insufficient pulse width of the trigger pulse but where additional triggers generated from a second pulse on the trigger line were not completely suppressed. Any additional trigger pulse before the reset signal for the APVm, or a trigger pulse wider than 25 ns, caused the FED to write the converted data another time into the buffer, quasi as a 'carbon copy event'.

From time to time also a trigger signal was generated in the idle loop of the data acquisition system leading to the conversion of the APVm bias level instead of an actual data frame (cf. trace (1) of Figure 11). Such a 'fake event' showed a signal overflow in all channels.

The rate of 'carbon copy events' and 'fake events' typically was less than 1 % and 0.1 %, respectively. The data quality was not spoiled by them as they could be identified and removed from the data sets later on in the off-line data processing.

Just to make it more complicated the LVDS trigger generation turned out to be temperature sensitive, both to the warm up after powering on the apparatus as well as to the ambient temperature. Above an ambient temperature of ∼25°C it became virtually impossible to find a setting which permitted proper data acquisition. Then the suppression of the second pulse at the end of the data frame failed and the rate of 'carbon copy events' increased to near 100 % inhibiting the taking of data.

For individual APVm chips the base line of the data frame showed a distortion shifting the channels at the beginning of the data frame to a higher DC offset from ground. As this effect was constant in time it only reduced the available dynamic range in a way which could be accepted.

A gradual DC shift with time of the whole APVm frame or just the channels of one MaPMT was observed in the case a ground line broke between the APVm and the FED input, usually in the special cables between the level adaptor and the FED. All affected data then had to be retaken.

Incompletly sampled signals: When the LED got charged by an electrical pulse it started to emit photons. For the available pulse width and heights of the trigger pulse the used LED emitted most photons within 100 ns. At a particular time delay after the trigger pulse it was most probable to observe a photon in the MaPMT. At this position usually the first photon was observed for the case that several consecutive photons from one pulse were detected by the MaPMT.

When using the APVm readout the system sampled the signal at this most probable position. The time jitter of the photons at this position was of the order of 25 ns, i.e. of the order of the sampling frequency. Therefore an a priori unknown fraction of LED pulses were not sampled by the APVm in or near the pulse maximum but rather on the flanks of the pulse. Such a bad sampling leads to a distortion of the MaPMT signal spectra filling up the region above the pedestal with events of underestimated signal

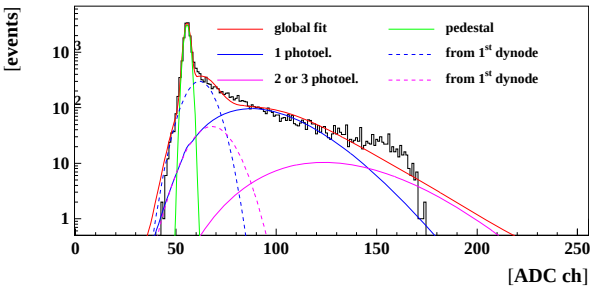

Figure 14: Upper gain limit of accepted fits; see text for explanation; this limit only was reached using the APVm readout with the 'no attenuation' configuration of the front-end board ("high-gain" resistor chain, 'no attenuation configuration', tube 9C20A2, pixel 10, HV = -680 V).

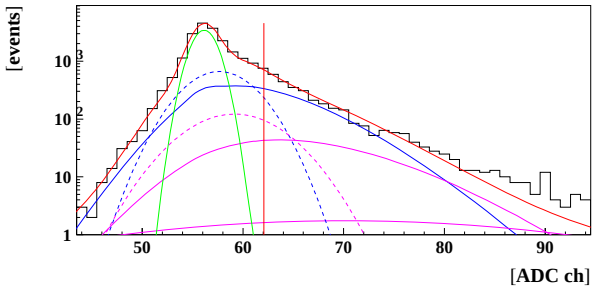

Figure 15: Lower gain limit of accepted fits; see text for explanation; in the zoom around the pedestal region also the $Q_0 + 5\sigma_0$ threshold is given as a vertical line ("high-gain" resistor chain, 'no attenuation configuration', tube 9C20A2, pixel 10, HV = -580 V).

gain. In the fitting algorithm used this region gets described by a hypothetical photo-conversion at the first dynode. In a fit to a single signal spectrum, like in the example given in Figure 13, the two effects can not be distinguished if there is not a clear peak in the data indicating a signal distribution with a lower gain. But form the experimental condition for the APVm readout one can expect that the contribution from the jitter is at least dominant.

The hypothesis of a photo-conversion at the first dynode therefore only could be tested with the CAMAC data. There the choice of a wide gate width of 200 ns should integrate over all consecutively emitted photons and is independent of an individual jitter. But the discussion in Section 6.3 will show that the hypothesis of a photo-conversion at the first dynode had to be rejected. The CAMAC data rather seem to suffer from incompletely sampled events as well. The only candidates for that would be very late photons which arrive at the tube when the gate gets closed.

5 Data Analysis

The raw data taken on a Windows NT platform was moved to a Linux system where the further data analysis took place.

For data taken with the CAMAC system a Fortran program was used to fill the raw data into a PAW ntuple without further modification. There were no dedicated pedestal runs as the pedestals were extracted from the signal spectra with a standard Gauss fit around the pedestal peak.

For the data taken with the APVm based readout each set of data runs was preceded by a pedestal run where the pulsing circuit to drive the LED had been switched off. Such a set of runs was analysed using a C++ program which first filled the pedestal run into PAW ntuples. Then for each channel the pedestal position and width individually was determined using a standard Gauss fit and stored for later use. Subsequent runs were subject to the following corrections before they were stored to PAW ntuples: (1) multiple consecutive copies of the same event and (2) events which only contained overflown channels - the 'carbon copy events' and the 'fake events' described in Section 4.3 - were identified and rejected and (3) an event-by-event common mode correction was applied.

For the common mode correction first the mean of all pedestal positions was calculated for all used channels of one front-end board using the fits of the pedestal run. Then for each event only those channels were selected which had no signal above the $Q\prime_0 + 5\sigma\prime_0$ threshold, with $Q\prime_0$ and $\sigma\prime_0$ the pedestal position and width according to the fit of the pedestal run. The mean of the selected channels then was taken as

an estimate of the actual mean pedestal position for this event. The difference to the reference value from the pedestal run then was subtracted from all values in this event.

Finally the log-file and run condition information was stored in a second ntuple which also provided space for the subsequently determined fit results on the signal spectra and the deducted signal loss. This latter ntuple had a common format for both, the CAMAC and the APVM readout system apart for the number of stored channels. This permitted the usage of the same software for the following analysis steps.

The histograms of the signal spectra were extracted and analysed using an improved fitting algorithm based on the Poisson distribution and the hypothesis of the contribution by a photo-conversion at the first dynode. This algorithm provides the best description of the signal spectra available and is discussed in detail in [13]. Typical good results of such fits are displayed in Figures 12 and 13 for CAMAC and APVm data, respectively. In the data the pedestal peak and the broad signal are clearly visible. The signal origines predominantly from single photoelectrons. The fit returned, N_{ev}, the overall normalisation, Q_0 and σ_0, the mean pedestal position and width, $\mu_{1,PC}$, the probability that one photoelectron is generated at the photocathode from photo-conversion, Q_1 and σ_1, the mean position above the pedestal and width of a signal distribution generated by single photoelectrons emitted from the photocathode, $\mu_{1,DYN}$, the probability that one photoelectron is generated from photo-conversion at the first dynode and finally Q_2 and σ_2, the mean position above the pedestal and width of a signal distribution generated by single electrons emitted from the first dynode. Using the fit result the signal loss due to a threshold cut at $Q_0 + 5\sigma_0$ then was calculated for the definitions $\ell_1, \ldots, \ell_5$ given in [13]. The contributions from up to three photoelectrons emerging form the photocathode (first dynode) are given as solid (dashed) curves in the Figures 12 and 13.

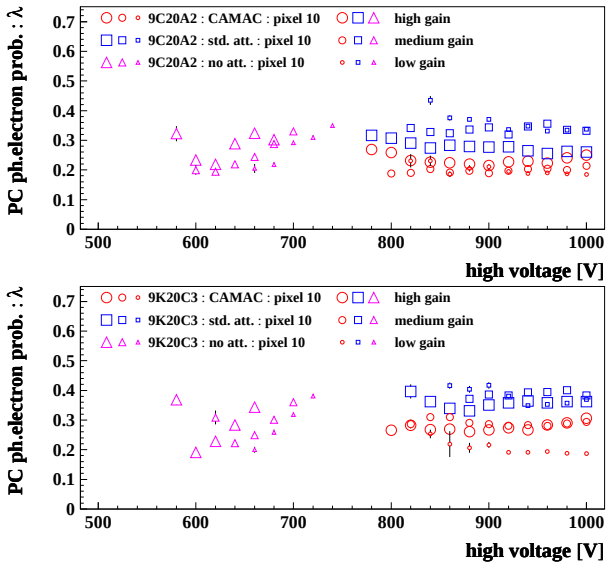

Figure 16: Control plot with the determined number of photoelectrons generated at the photo cathode for the accepted data points for several data sets; top: old focusing tube 9C20A2, bottom: new focusing tube 9K20C3.

A particular concern was the setting of the start parameters in the fitting procedure. As the supply voltage was varied by 300 V in a scan for a particular readout option the variation of the resulting signal spectra extended over the full available dynamic range. There was no universal set of start parameters which would allow converging fits which were leading to a proper descriptions of the data in all cases on such a range of spectra. In order to minimise the arbitrariness in the choice of the start parameters and the risk of influencing the final result by that the parameters were calculated using the following automatic procedure: (1) the runs were ordered in descending supply voltage as they were taken in voltage steps of 20 V, (2) the run with the highest HV setting, i.e. with the highest signal gain, was fitted first using a specific set of starting parameters as described below, (3) the run with the next lower setting inherited the fit results of the previous run as start parameters and (4) the last step was repeated till the end of the run series. For the first run of a series the start values of N_{ev} and Q_0 were taken as the number of entries in the histogram and the histogram channel with the maximum of entries, respectively. For the other parameters a set of typical fit results for spectra filling the whole dynamic range was used. Once established in manual test fits this set was used as start condition throughout this study, scaled for the different resolutions of the used ADCs in the CAMAC and APVm readout.

With each step of 20 V reduction of the supply voltage the MaPMT gain then was found to be reduced by about 25 %. This was small enough to lead reliably to a good description of the signal spectrum of the next run when the fit results of the previous run were inherited as start parameters.

The automated fitting procedure resulted in a few fits with abnormal large numerical errors on some of the parameters, although the description of the data in these cases was good. This is a known flaw when using PAW as fitting environment. For the affected histograms the fit was iterated using the two most significant digits of the found fit values as start parameters. This always lead to error sizes comparable to the other fit results while the new parameter values were close to the previous ones, i.e. well within the size of the new errors.

All fitting results were visually inspected using plots as shown in Figures 12 and 13 to judge the

quality of the fit. Figures 14 and 15 demonstrate the very limits to which the fits were accepted for further analysis.

In Figure 14 one can see an example with a low upper limit of the dynamic range of the FED. It starts to cut away the events with large gain. In more extreme examples with higher signal gain the region below this cut showed a distinct, nonphysical peak of entries. It stemmed from events with a true charge larger than the high-gain cut-off. Apparently, for such events the APVm saturated and the excess charge distorted the signal shape in a way that the signal was not sampled with a fixed value at the top of the dynamic range but rather scattered around in the upper region. Such a peak of scatterd samples due to an excess charge just starts to build up in Figure 14 as well. This limit was only reached in the measurements using the APVm readout with the 'no attenuation' configuration of the front-end board.

Figure 15 shows the limit of low gain where the MaPMT signal still can be reasonably described by the fit method before the superposition with the pedestal leads to an arbitrary result of some or all fit parameters. This limit was determined by observing the continuity of all the fit parameters over the high voltage scan. The determined number of photoelectrons generated at the photo cathode turned out to be the most sensitive parameter. From the point the continuity of the fit parameters was broken for an individual data set the data points were disallowed for the final results. For a selection of data sets Figure 16 shows a compilation of the determined number of photoelectrons and gives an idea of this selection.

The results presented in this study base on the accepted fit results and the quantities derived from the fit parameters. The errors of the fit parameters were propagated in the calculation of the derived quantities. The experimental error of the high voltage was $\pm 0.5\,\mathrm{V}$ for the relative uncertainty between the voltage levels. The resulting errors always are plotted but usually are smaller than the symbol sizes.

6 High Voltage Scans

In the following the results are presented for the behaviour of the signal response of the MaPMTs when the supply voltage is varied over the full range available. The results are compared for the three readout systems: CAMAC based, APVm based with standard attenuation and APVm based with bypassed attenuation. Each of the three systems was studied with the three gain options defined by the used resistor chain: "high-", "medium-" and "low-gain". In addition it was looked for possible differences in the results for the two types of focusing in the MaPMT (old: tube 9C20A2; new: tube 9K20C3) or in the behaviour of border pixels to inner pixels. No significant differences were found in these cases.

6.1 Signal Gain

In Figure 17 the gain of a single photoelectron signal is plotted versus the negative high voltage applied to the MaPMT. The data is plotted in units of ADC channels as returned by the fit. The pedestal subtraction has been applied. Displayed are the found gain values for one particular pixel of the tubes 9C20A2 and 9K20C3, respectively. Due to the different readout hardware the various readout options cover different areas in the plane. Figure 17 compiles all the accepted fit results for the various data runs on the pixels displayed.

For a given readout option the single photoelectron signal, i.e. the gain of charge in the tube, increases exponentially with the negative supply voltage. For a quantitative description exponential fits of the form $gain = e^{a+bV}$ were applied to the individual data sets. These are also plotted in Figure 17. The fit ranges were limited towards lower supply voltages where the gain behaviour was not anymore well represented by an exponential description but dropped faster towards smaller values of applied voltage; an effect which has to be assigned to the photon signal spectra being less well distinct from the pedestal in this regime. An example of such signal spectra at the worst case limit of this regime can be seen in Figure 15.

The fit results were averaged over the tested gain options, the used tubes and channels. For the CAMAC readout in average the gain doubles with every increase of $\Delta V_{CAMAC} = 47\,V$ with a variance of $\sigma_{\Delta V} = 1.5\,V$. The corresponding numbers for the standard APVm readout and the APVm readout with bypassed attenuation are: $\Delta V_{APVm,std} = 60\,V$, $\sigma_{\Delta V} = 4.2\,V$ and $\Delta V_{APVm,noatt} = 58\,V$, $\sigma_{\Delta V} = 12\,V$, respectively. In all three cases the distribution of the ten to twelve contributing values around the averages ΔV is consistent with a Gaussian distribution.

The fact that the $\sigma_{\Delta V}$ is so small for the CAMAC readout is a result of the fits of the signal spectra being so well under control in the range where the exponential fits were applied to the data sets. The coarser 8-bit resolution of the ADC used with the APVm readout with respect to the 10-bit CAMAC ADC might account for some of the relative increase of $\sigma_{\Delta V}$ for the standard APVm readout. But the main cause is that, although the individual signal spectra are fitted well, the overall gain behaviour with varied

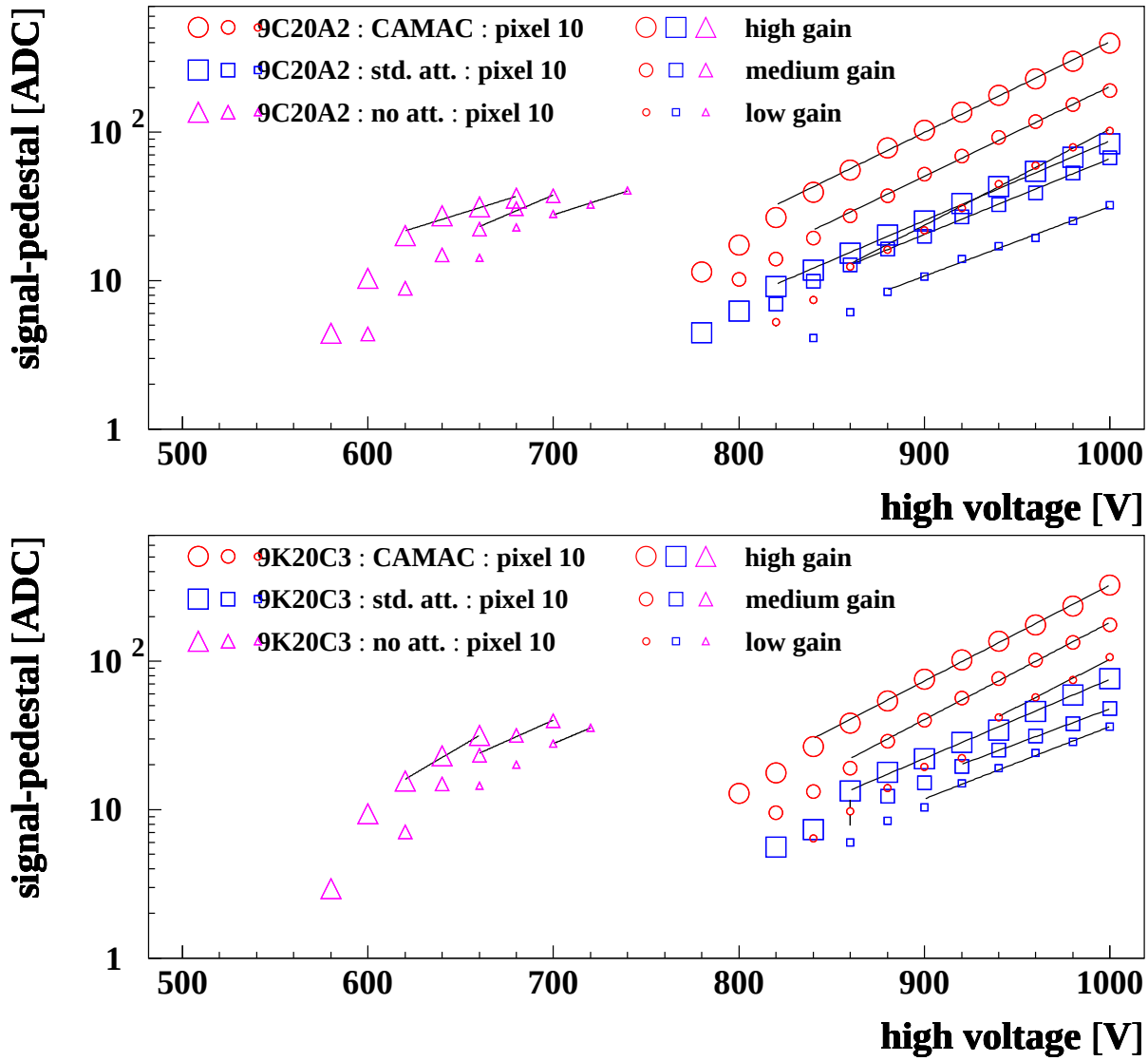

Figure 17: The gain of a single photoelectron signal above pedestal as returned by the fit, shown for pixel 10 of tube 9C20A2 (top) and tube 9K20C3 (bottom) and all the readout options available; the lines represent exponential fits ($gain = e^{a+bV}$) to selected ranges of the data sets.

high voltage is not as well described by an exponential function as in the case of the CAMAC readout. This is significantly worsened for the APVm readout with bypassed attenuation by two circumstances. The quality of the signal spectra is poor compared to the other readout systems, i.e. the features of the signal spectra are less distinct at the same gain. Therefore the fits of the spectra are less reliable. This is illustrated in Figure 18 which gives a comparison of the signal spectra and their fits at similar gain using the "low-gain" option in the standard APVm readout and the APVm readout without attenuation. In addition the overall limitation in the dynamic range for the APVm readout without attenuation causes the range to be very small where the gain behaviour can be described well by an exponential. Therefore the $\sigma_{\Delta V}$ depends in this case much more on single spectra.

The conclusion from the quoted ΔV and $\sigma_{\Delta V}$ values is that the measured gain behaviour is the same for the two APVm based systems. But when measured with the CAMAC system the slope of the exponential is about 25 % larger. The MaPMT tubes are expected to behave in the same way independent of the data acquisition system used, i.e. this finding points towards a significant difference in the linearity of the CAMAC and the APVm system. Although such a large difference is beyond the tolerances of the used amplifiers and ADCs an 'out-of-boundary' behaviour of one of these components is assumed to be the most likely culprit. The attenuation network can be excluded as it is only used in one of the APVm systems and the known problem of the jitter of the LED signals present in the APVm system cannot account for that as well as the jitter is not correlated to the signal size. The reason for this discrepancy

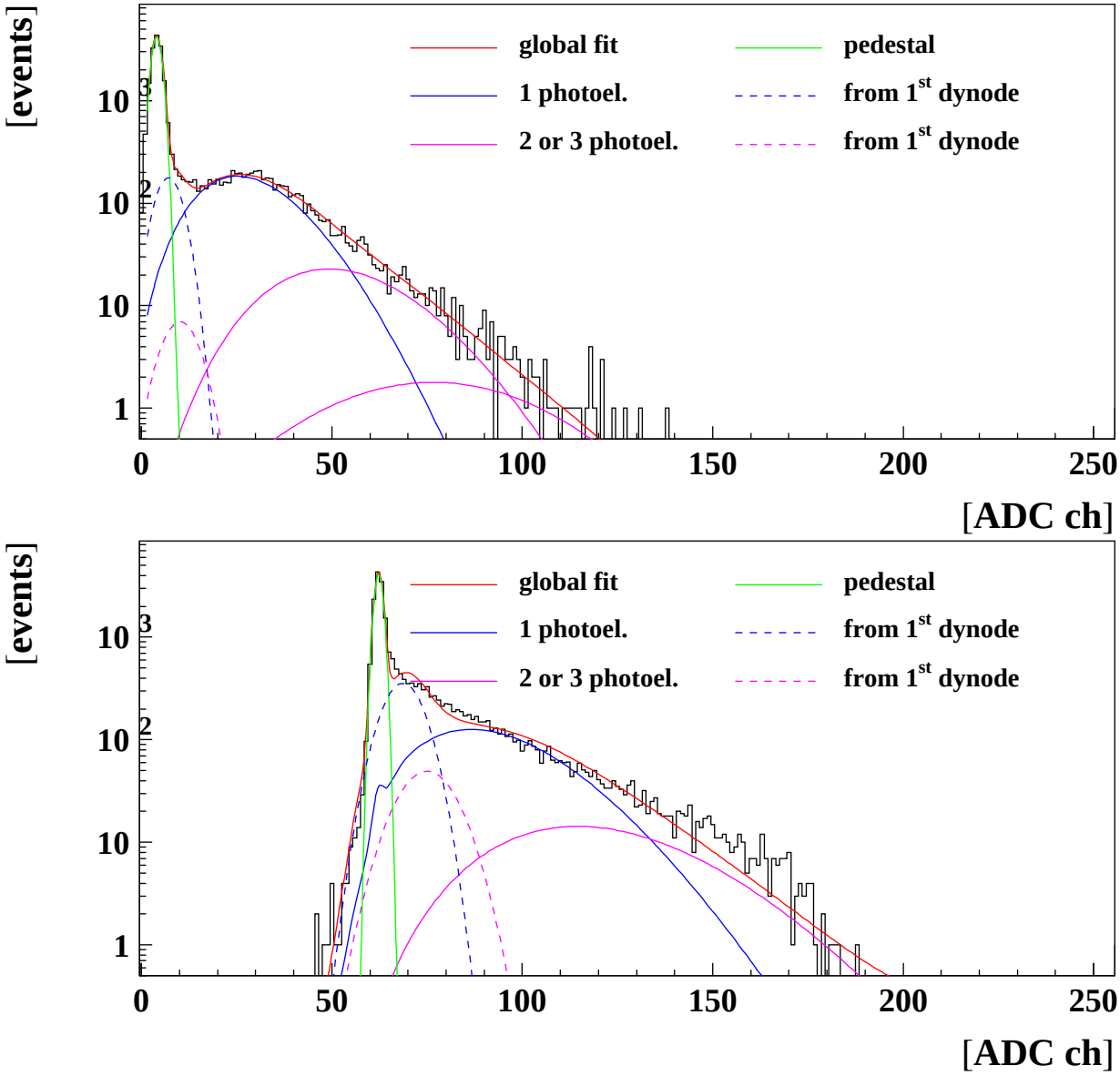

Figure 18: Signal spectra with similar gain taken with the standard APVm readout (top) and the APVm readout without attenuation (bottom) using the "low-gain" option for pixel 10 of tube 9K20C3; taken at 960 V and 700 V, respectively.

remains unresolved as there is no data available at this time to calibrate the linearity of either of the two systems. It is especially not clear whether this problem is located in the CAMAC or in the APVm system.

The relative behaviour of the three gain options, "high-", "medium-" and "low-gain", was established by calculating the ratio of the single photoelectron gains found for any pair of the gain options at a given supply voltage individually for each readout system, tube and pixel. Any pair with both fit results among the accepted data points was regarded. For each of these individual data sets the gain ratios were averaged over the range of the supply voltage. In a second step the data was averaged over the available pixels in each MaPMT tube, eight pixels in the case of the CAMAC readout and two pixels for each of the APVm readouts. These values are presented in Table 3 together with an additional average over the two MaPMT tubes. The value of the "high-over-low-gain" ratio for the tube 9C20A2 using the CAMAC system (3.90) is derived from data taken with the same hardware and run conditions as the data sample lost in a disk crash which was used to calculate the corresponding ratio (3.9) in the previous study [12]. A similarity in the values well within the errors is expected, the actual match of the values is by chance.

The tendency of larger errors for the CAMAC system reflects the larger number of pixels available compared to the two other systems which seem to have the same pixel-to-pixel variation. For the APVm system without attenuation the range of supply voltage available for the ratio typically is very small and

	CAMAC	APVm std.	APVm no att.
# pixel	8	2	2
average over tube 9C20A2			
hi/me	1.74 ± 0.42	1.25 ± 0.04	1.87 ± 0.08
me/lo	2.17 ± 0.31	2.00 ± 0.05	1.62 ± 0.29
hi/lo	3.90 ± 0.73	2.47 ± 0.13	2.89 ± 1.41
average over tube 9K20C3			
hi/me	1.88 ± 0.14	1.48 ± 0.00	1.50 ± 0.39
me/lo	1.62 ± 0.38	1.34 ± 0.01	1.54 ± 0.01
hi/lo	3.06 ± 0.52	2.00 ± 0.04	1.97 ± 0.30
total averages			
hi/me	1.81 ± 0.31	1.36 ± 0.13	1.67 ± 0.31
me/lo	1.90 ± 0.44	1.67 ± 0.38	1.58 ± 0.17
hi/lo	3.48 ± 0.75	2.24 ± 0.28	2.43 ± 0.98

Table 3: Average gain ratios for the "high-gain" (hi), "medium-gain" (me) and "low-gain" (lo) resistor chain option given for the used readout systems and the two MaPMT tubes 9C20A2 and 9K20C2 separately and as total average; also given is the number of pixel averaged over per tube.

hence the quoted ratios and errors are less reliable than for the other two cases.

Two observations can be made from these ratios in Table 3. The tube 9K20C3, with the improved focusing, seems to respond with a lower gain change to a change in the resistor chain than the tube 9C20A2, the one with the old focusing. This $1\sigma \ldots 2\sigma$ effect might indicate a lower sensitivity to potential changes between the photo cathode and the first dynode for the newer tube type. It could be due to the changed electrical focusing field in this area which had the aim to make the collection of photo electrons from the photo cathode more robust. But unless this is confirmed by the measurement of additional MaPMT tubes this is indistinguishable from a simple tube-to-tube variation. Therefore also an average over the tubes is given in Table 3.

Secondly one can observe that the gain response to a change of the resistor chain generally is larger for the CAMAC system than for the APVm system separating the results by about 2σ. This can be explained by the $\approx 25\,\%$ difference in the linearity of the CAMAC and the APVm system as found in the exponential fits of Figure 17. In these fits a gain ratio R_g translates into a voltage difference ΔV as: $\Delta V = \ln R_g / slope$. Thus, if the slope of the exponential behaviour is changed, e.g. to recalibrate the system, R_g scales logarithmicly with the slope: $\ln R_{g,scaled} = f * \ln R_g$, with f being the scale factor of the slope. By rescaling of either set of values in Table 3 with a factor of 25 % in this way the difference found for the CAMAC and the APVm system is reduced and the scaled values become compatible just within the 1σ margin. This is not completely satisfying as the scaled values still seem to consist of two classes rather separated by 1σ than scattered within the errors. But this residual difference cannot be resolved with the data available and there is no cause obvious which could account for that. So for now the 25 % difference in the slopes is taken as the only cause.

6.2 Gain Calibration

To quote the absolute signal gain ranges covered by the different readout options an 'ADC channel-to-charge' calibration has to be performed for each system. Only for the CAMAC ADC an absolute charge calibration is known from the specifications: the charge range is $256\,pC \pm 0.5\,\%$ into 1024 ADC channels. This corresponds to $0.25\,pC \pm 0.5\,\%$ or $1.560 \times 10^6 \pm 7.800\ e^-$ per ADC channel. The signals were amplified by two stages of amplifiers between MaPMT and ADC with a gain of $\times 10 \pm 2\,\%$ each giving a total of $\times 100 \pm 4\,\%$ amplification. The size of this error was verified for the used system by applying a constant test charge to each of the used readout channels. It dominates the error on this calibration. The calibration constant for the MaPMT signals measured with the CAMAC system calculates to $15600 \pm 630\ e^-/ADCch$.

No absolute calibration was available for the APVm⊕FED system. Thus an inter-calibration had to be generated from the comparison of the signal response measured with the CAMAC and the APVm⊕FED system to the same signal source. No data with electronic calibration pulses were available. So the fitted values of the single photoelectron gains were chosen as the signal for this comparison. The measured gains, in ADC channels, were derived from the data taken with the CAMAC and the standard APVm system at the same run conditions, i.e. using the same tube, pixel, gain option and high voltage. For one particular pixel of one tube the results are summarised in Figure 19.

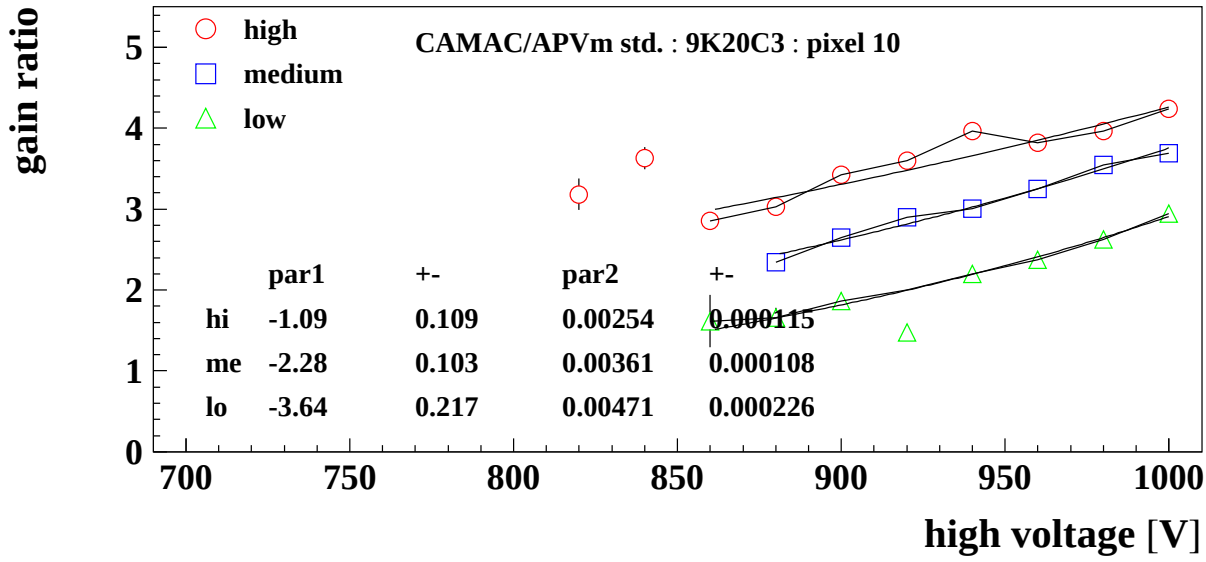

Figure 19: Ratios of gains measured with the CAMAC and the standard APVm system using the same run conditions given for pixel 10 of tube 9K20C3 using the three gain options; also quoted are the parameters of an exponential fit $gain\,ratio = e^{par1+par2*V}$.

Two components contribute to the found ratios. A factor of $\times 4$ just reflects the relative amount of ADC channels of the CAMAC ADC and the FED. The visible deviations to such a constant ratio arises from the difference in the linearity of the two systems. Also the fact that the gain ratios for the three gain options in Figure 19 do not fall onto one curve is caused by that. This happens here in exactly the same way as discussed for the average gain ratios in Table 3 as here the same data is just reordered into new ratios. Exponential fits of the form $gain\,ratio = e^{par1+par2*V}$ were applied to the data[3] of the three gain options as shown in Figure 19. For these fits similar range limitations were used as they were discussed for the exponential fits in Figure 17 but occasionally allowing one or two more data points towards lower supply voltages. In effect the fits parameterise the found $\sim 25\,\%$ difference in the slopes of the gain behaviour presented in Figure 17 for the CAMAC and the standard APVm system.

As it is not determined which of the systems has to be regarded as the reference with respect to the linearity problem in this study calculations always has been done for both cases. Either the APVm data was scaled to match the CAMAC data. In this case the calibration quoted above for the CAMAC system could be applied to the APVm data as well. Or the CAMAC data and with it the quoted calibration was scaled towards the APVm data. This resulted in considerably larger MaPMT anode signals for the measurements at low values of the supply voltage. Figure 20 shows the charges at the MaPMT anode measured with a particular pixel of one tube calibrated in both ways. This Figure is generated from the same data as the bottom plot of Figure 17. Figure 20 demonstartes that the scaling projects the data sets for the CAMAC and the standard APVm system very nicely onto each other.

To find a calibration for the data taken with the APVm readout without attenuation an extrapolation has to be performed between the data sets using the standard APVm system and the APVm system with bypassed attenuation as there is no overlap. Such an extrapolation was justified as the two systems had been found to have the same gain behaviour. The a priori unknown parameter in this extrapolation was the actual attenuation factor imposed by the RC network which was used in the standard APVm readout. The attenuation factor, originally designed to be ~ 10, turned out to be rather ~ 30 for the investigated channels. Such a factor is still plausible within the tolerances of the used capacities and taking into account the additional capacities apart from the Kapton cables. In Figure 20 an attenuation factor of 30 ± 6 was assumed which leads to a good match of the two data sets on common exponential curves. The $20\,\%$ error on this factor was estimated as a reasonable limit to which this factor could be estimated by such an extrapolation procedure. This error is included in the errors plotted for the data points in Figure 20 for the APVm system with bypassed attenuation.

Averaging first over the available data for different tubes and pixels and then also combining the

[3] As the only exception in this procedure the value at 920 V for the "low-gain" option actually was cheated before applying the fit. Without that the fit would have been dragged low by the signal spectrum of this single run in the CAMAC series which drops out of the general gain behaviour. It would have spoiled the description of the other data points in Figure 19.

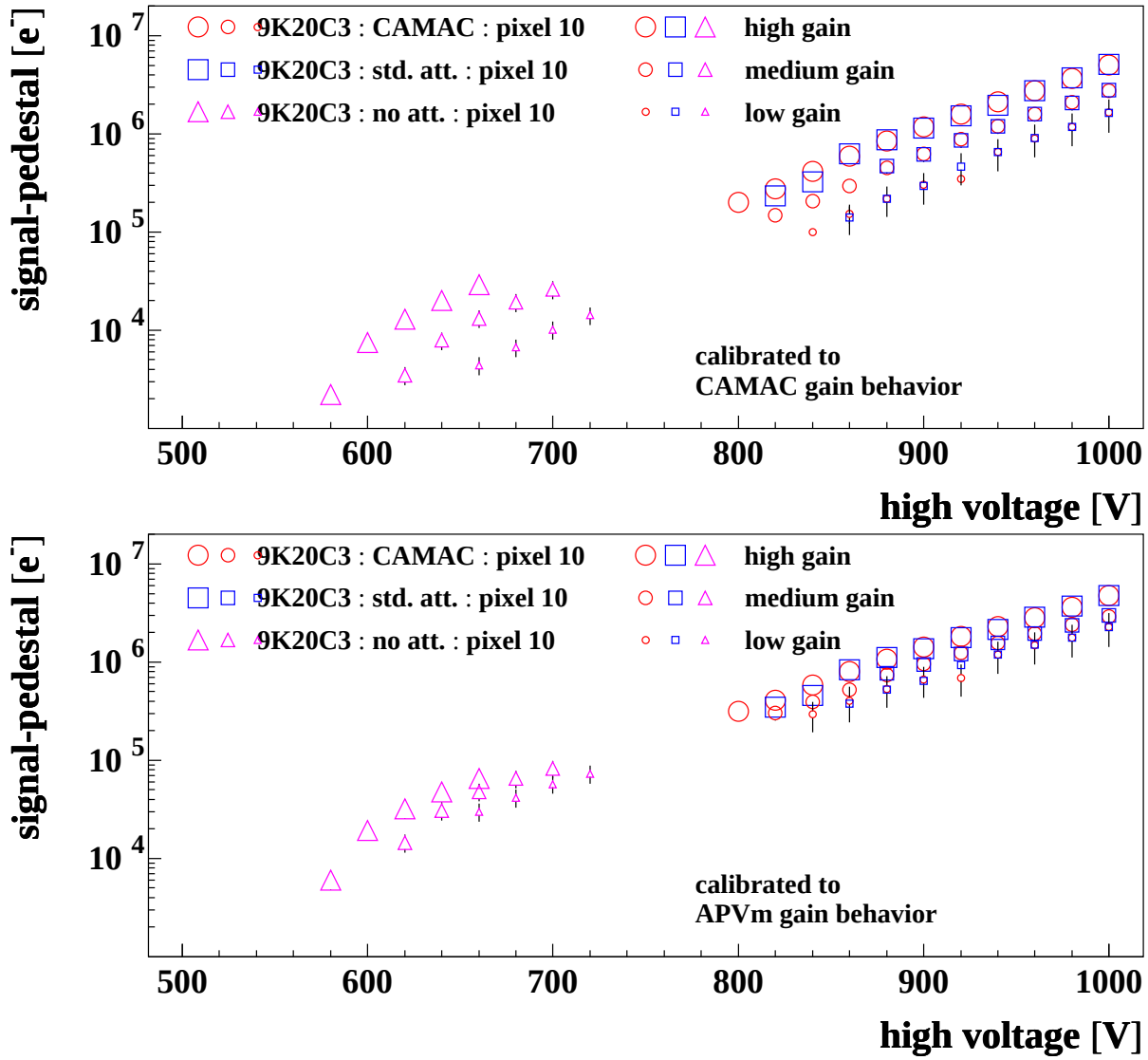

Figure 20: MaPMT anode signals from the data of the bottom plot of Figure 17 (pixel 10 of tube 9K20C3) calibrated to e^-; shown under the assumption that the CAMAC system (top) or the standard APVm system (bottom) provides the right linearity.

in $10^3 e^-$	600 V	660 V	700 V	760 V	800 V	860 V	900 V	960 V	1000 V
calibrated to CAMAC gain behaviour									
high	12.3	32.0	60.6	↔ 149.	272.	673.	1230.	3050.	5580.
medium	4.54	12.5	24.5	67.4	132.	363.	↔ 687.	1690.	3090.
low	2.75	7.41	14.3	↔ 32.8	63.1	168.	324.	866.	1670.
calibrated to APVm gain behaviour									
high	27.8	59.2	97.9	↔ 221.	372.	810.	1360.	2970.	4980.
medium	20.4	45.1	76.7	170.	288.	639.	↔ 1100.	2170.	3410.
low	17.8	34.7	54.0	↔ 112.	184.	385.	630.	1320.	2160.

Table 4: Calibrated charge response of MaPMTs to single photoelectrons, in $10^3 e^-$, given for the three used gain options and both discussed calibrations; the values are extrapolated from the fits of Figure 21 and the arrows indicate whether they are extrapolated from data using the APVm system without attenuation (left of the arrow) or the combined CAMAC & std. APVm data (right of the arrow).

in $10^3 e^-$	500 V	550 V	600 V	650 V	700 V	750 V	800 V	850 V	900 V	950 V	1000 V
Hamamatsu data sheet											
default	2.2	5.9	14.	35.	74.	160.	300.	560.	1100.	1800.	3300.

Table 5: Gain of MaPMTs to single photoelectrons, in $10^3 e^-$; from Hamamatsu data sheet.

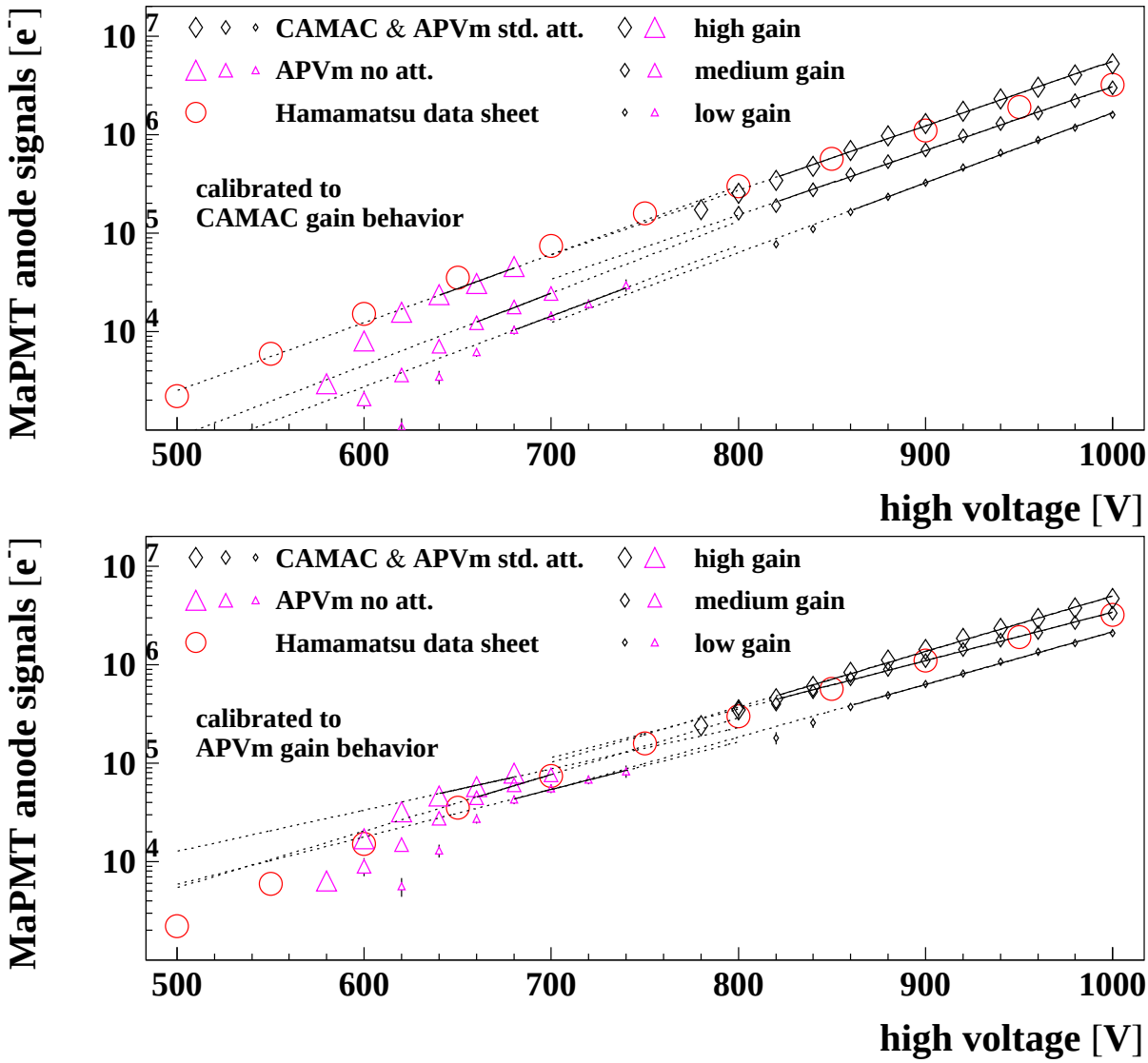

Figure 21: MaPMT anode signals after averaging over the available data for the assumption that the CAMAC system (top) or the standard APVm system (bottom) provides the right linearity; exponential fits are applied (solid lines) and extrapolated (dotted lines) and Hamamatsu data are shown.

data from CAMAC and the standard APVm readout leads to the representation in Figure 21. Again exponential fits are applied (solid lines) and in addition their extrapolations are given (dotted lines). The extrapolations confirm the good match of the two data sets with an assumed value of 30 ± 6 for the attenuation factor and represent the best visual match found for the checked values of 10, 15, 20, 25, 30, 35 and 40 for the attenuation.

In addition the gain curve quoted in the Hamamatsu data sheet is reproduced in Figure 21. Hamamatsu quotes it for the default resistor chain, i.e. it compares directly to the "high-gain" option. The Hamamatsu data does not follow an exponential with a constant slope but the slope decreases with increasing supply voltage. In contrast the data presented here exhibits a relatively constant slope over a wide range and thus does not match well the Hamamatsu data in either of the two calibration representations used. The fact that the MaPMT gain actually can be measured as much better approximation to an exponential than shown by the Hamamatsu data leads to the conclusion that the change of slope in the Hamamatsu data is likely to be imposed by effects in the electronics rather than within the tube. Therefore a comparison to the Hamamatsu data is not distinctive to judge which of the used calibrations is the better one.

Using the fits on the averaged calibrated data the average charge response of MaPMTs to single photoelectrons was calculated for a sample of values of supply voltage. The findings are summarised in Table 4 separated for the three used gain options and the two ways of calibration. For comparison the values read from the Hamamatsu data sheet are given in Table 5. In Table 4 it is also indicated

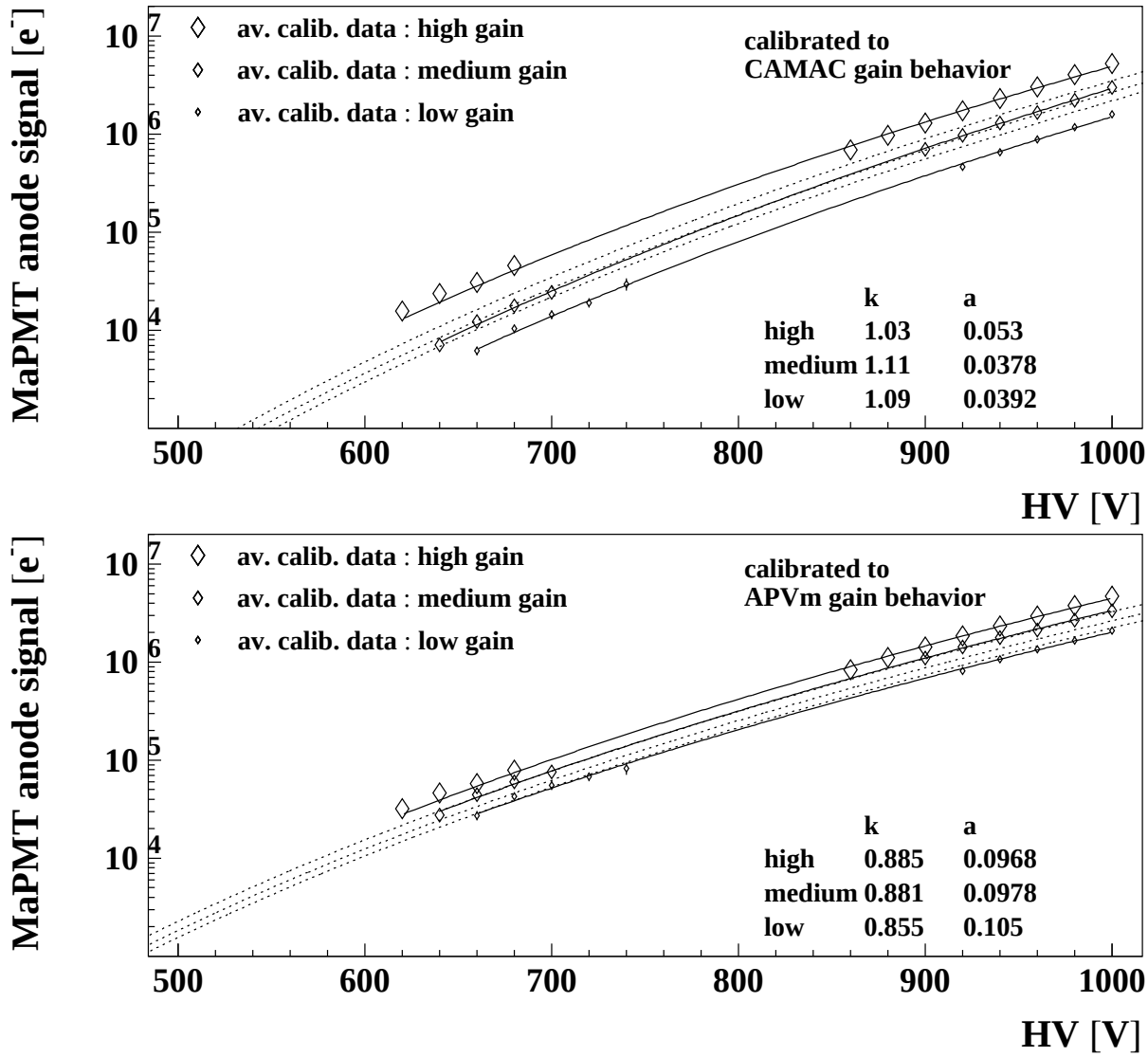

Figure 22: Fit results (solid lines) for the gain model applied to the averaged and calibrated MaPMT anode signals from Figure 21 together with the results on the free parameters k and a; gain model with universal parameters (dotted lines) from averages of the found k and a.

whether the values are extrapolated from data using the APVm system without attenuation or form the combination of data using the CAMAC and standard APVm system. For the latter case the averages for the "medium-gain" data got pulled high by two data sets with relatively large values in the region below 900 V. The effect on the fit can clearly be seen in Figure 21. Therefore in this case in Table 4 the boundary between the two extrapolations was pushed to higher values of supply voltage.

6.3 Gain Model

In order to understand better the internal gain behaviour of the MaPMTs a gain model was applied to the data sets. In this model the gain of electrons at dynode x is $g_x = a \cdot dV_x^k$, with the potential dV_x before dynode x, a material dependent constant, k, defining the slope of the gain and a normalisation constant a. The total gain of a MaPMT then is $g_{tot} = \prod_{x=1}^{n} g_x$, with n the number of dynodes in the tube. This was implemented into a fitting routine leaving k and a as free parameters while n and the values of the actually used resistor chain, cf. Table 1, were given as input to compute the dV_x at a given supply voltage V. The fitting procedure turned out to be very sensitive to the chosen start values of k and a with the tendency to run into local minima. Therefore an input parameter scan with fine step size was performed where finally the result with smallest χ^2 was chosen while the individual fits used the maximum likelihood method. Figure 22 presents the fit results obtained by applying this algorithm to the averaged and calibrated data presented in Figure 21. The fits use all the data points shown in Figure 22.

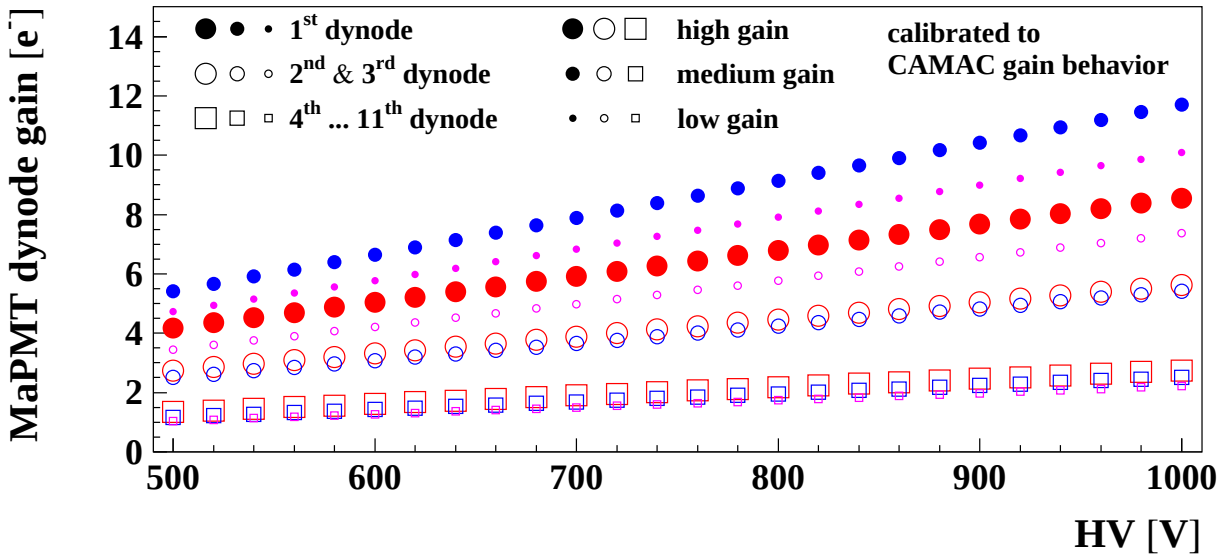

Figure 23: Gain at MaPMT dynodes from the gain model fitted to the data in Figure 22.

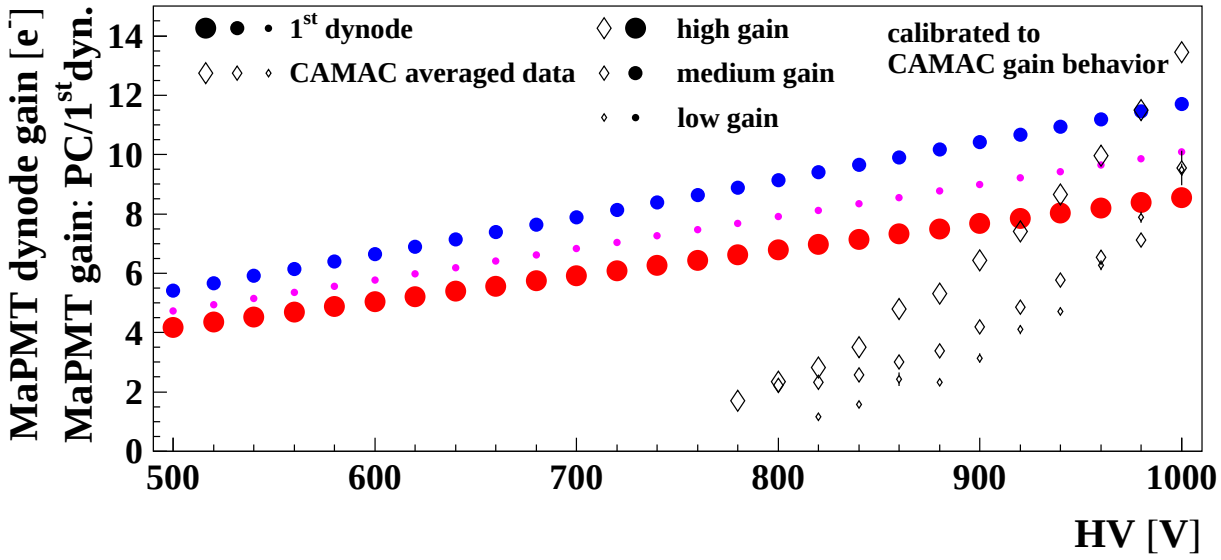

Figure 24: Comparison of gain at first dynode from model with the ratio of gains found in the fits to CAMAC data for photoelectrons generated at the photocathode or supposedly generated at the first dynode.

They represent the data well over more than two orders of magnitude in the size of the signal.

From the found values of k one can conclude that the slope of the gain can be described by a universal parameter for the three gain options, being $k \approx 1.08$ provided the CAMAC based calibration is correct and $k \approx 0.87$ if the APVm based calibration is correct. Hamamatsu quotes a value range of $k = 0.7 \ldots 0.8$. This is consistent with the data quoted by Hamamatsu and shown in Figure 21 where in the range $800 \ldots 1000\,\mathrm{V}$ the slope of the MaPMT gain is smaller than for the data presented in this study. As discussed this is likely to be caused by the different electronics.

If now also the normalisation a is made universal the model fails to describe the consequences of changes to the resistor chain as one can see from Figure 22 as well. There the gain model is given for averaged k and a parameters as dotted curves. In this case the separation between the gain options is underestimated by a factor of ~ 3.

Despite of the caveat that a can not be regarded as universal the gain model still can be used to understand the gain behaviour along the dynodes within a MaPMT. Figure 23 displays the gain at the dynodes of the MaPMT as obtained from the fits of the top part of Figure 22. The gains scale with the

supply voltage almost linearly as $k \sim \mathcal{O}(1)$. The relative behaviour of the three gain options turns out as can be expected from the changes made to the resistor chains. The "medium-gain" option has a strongly increased g_1 with respect to the "high-gain" option while the gain at all other dynodes is slightly reduced. For the "low-gain" option the gain is moderately increased for the first three dynodes with respect to the "high-gain" option while the the gain of the further dynodes is decreased stronger.

The absolute values of the gains look reasonable as well. For example for the "high-gain" option a gain at the first dynode is found to be $g_1 = 6.8$ at a supply voltage of 800 V which raises to $g_1 = 8.6$ at 1000 V while the potential before the first dynode is 109 V and 136 V, respectively. It means that in average a potential of ≈ 16 V is needed to emit a secondary electron from the semiconductor surface of the dynode, or - by assuming a band gap of $\mathcal{O}(4\,\mathrm{eV})$ - the probability of the release of a secondary electron into the vacuum is $\sim 1/4$. This relation generally holds for any other dynode and any supply voltage distribution to them, i.e. any chosen gain option, in the data presented. It represents constant material behaviour for the semiconductor coating of the dynodes.

In Figure 24 the gain at the first dynode as it comes out of the model is compared to the ratio of gains found in the fits to CAMAC data for photoelectrons generated at the photocathode or supposedly generated at the first dynode. The model behaviour was compared to averaged CAMAC data only as there the dilution of the assumed photo-conversion at the first dynode by a jitter of the light pulses was thought to be negligible compared to the APVm data sets. The finding is that even for the CAMAC data the ratio between the two contributions to the MaPMT signal is in fundamental contradiction to the model prediction for the gain at the first dynode. Neither reflects the data the relative size of the gain at the first dynode for the three gain options. In the data the order just reflects the total gain of a signal of a single photoelectron produced at the photocathode but not the increase of the potential before the first dynode for the two options with reduced total gain. Nor reproduces the data a compatible behaviour with the supply voltage. The ratio in the data falls much faster than the gain at the first dynode for reduced supply voltage and approaches 1 at around 800 V where the MaPMT signal size approaches the magnitude of the electronic noise.

So, in spite of the fact that the region between the pedestal and the single photoelectron peak in the signal spectrum can be successfully parameterised by an assumed photo-conversion at the first dynode and in spite of the fact that individual signal spectra seem to exhibit a broad peak in this region this contribution to the signal must have a different origin. It does not scale like a signal originating from a single electron emitted from the first dynode but does scale like signal originating from an electron produced at the photocathode. In the APVm data a contamination of incompletely sampled signals is known to be present as discussed in Section 4.3. This data shows similar behaviour as found here for the CAMAC data. Therefore it is suspected that the signal contribution between pedestal and single photoelectron peak in the CAMAC data is caused by incompletely sampled signals as well. But since the used gate width was 200 ns only delayed light pulses can contribute here opposed to the jitter of the main LED pulses which are important for the APVm readout. Only further tests with an improved light source will be able to confirm or falsify this interpretation of the source of the signals below the single photoelectron peak. But it can be concluded that with none of the three used readout systems a signal contribution was found which would be consistent with a photo-conversion at the first dynode.

6.4 Signal Loss

The amount of loss of the MaPMT signal due to a threshold cut depends on the ratio of signal-over-noise, S/N. The higher the S/N the lower the loss of signal can be kept which is caused by a cut on the signal hight. In this study the cut to distinguish signal from noise was defined to: $S > Q_0 + 5\sigma_0$, using the pedestal position Q_0 and its width σ_0 as parameters to measure the electronic noise in the particular readout system. The position of this cut is indicated by a vertical line in the example spectra given in the Figures 12, 13 and 15.

For an individual data set the pedestal width stays constant. Therefore within each data set the signal loss increases with decreasing gain of the signal, i.e. with decreasing S/N. But for different data sets the pedestal widths may vary due to the different experimental conditions. The typical noise levels for the data sets used in this study are displayed in Figure 25 for an example subset. The noise levels found generally fall into the region of $\sigma_0 = 1.1 \ldots 1.4\,ADC$ channels and are reasonably constant for individual data sets. For the CAMAC data generally a $\sigma_0 \approx 1.4\,ADC$ channels was measured. For the standard APVm system $\sigma_0 \approx 1.1\,ADC$ channels was determined by the fits. For the APVm system with bypassed attenuation typically a σ_0 comparable to the CAMAC (standard APVm) readout was found when using the "high-gain" ("low-gain") option. When the "medium-gain" option was used various levels of noise were found between these two limits. Therefore the individual fits to the signal spectra of the APVm

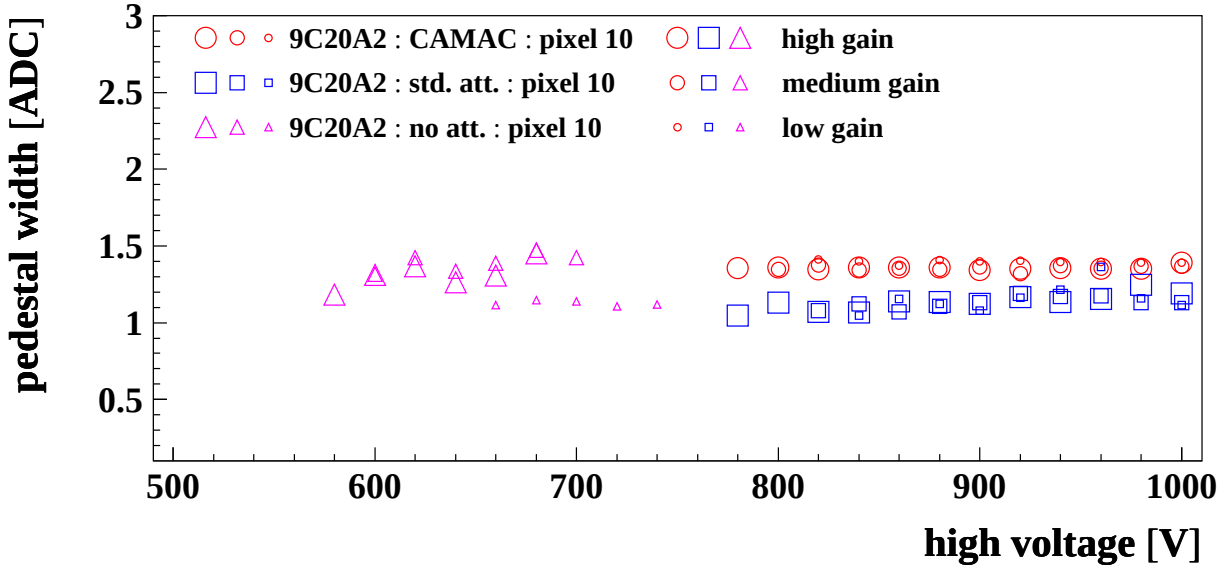

Figure 25: Typical noise levels for the used data acquisition systems; in *ADC* channels as derived from the fits of the signal spectra; for the same data as in the top part of Figure 17.

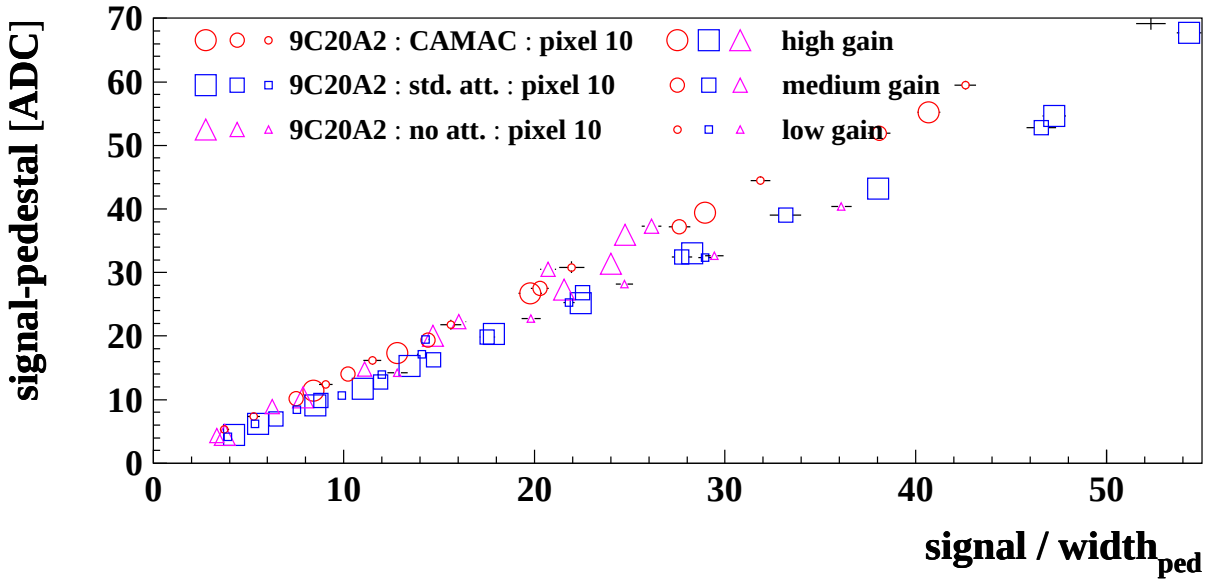

Figure 26: The gain of a single photoelectron signal plotted against the signal-over-noise in the particular readout system; this is the same data as in the top part of Figure 17 zoomed into the region of smaller signal-over-noise.

readout with bypassed attenuation were rechecked in detail and for most spectra it was found that the fitted pedestal width represented the actual data well. Only at the limit of low gain, i.e. at low supply voltage, the so called "first dynode" contribution to the fit started to accrete events off the pedestal and thus to artificially reduce σ_0. This is visible in the example spectrum displayed in Figure 15 as well.

The variation of the pedestal width between the data sets leads to a corresponding variation of the S/N behaviour. Figure 26 plots the gain of a single photoelectron signal, as derived by the fit to the signal spectra, against the S/N in the particular readout system for data sets of Figure 25. It turns out that the standard APVm readout typically has a S/N which is about 20 % higher than for the CAMAC readout at the same gain, independent of the chosen gain option. This corresponds well to the found pattern in the electronic noise levels. The S/N found for the APVm readout with bypassed attenuation follows the pattern found in the pedestal widths as well.

In order to make a proper comparison of the various readout options the loss, ℓ, is plotted against S/N, the quantity the loss depends on. This way the minimum value of S/N needed to keep the signal

loss below a given limit becomes obvious. Also the readout options can be compared easily this way.

In the following discussion the loss definitions ℓ_5 and ℓ_3 defined more precisely in [13] are used. Also confer to Figures 12 and 13 to better understand the following brief description. The definition ℓ_5 defines signal loss as that fraction of the single photoelectron contribution to the signal spectrum which is below the threshold cut. In this definition only photoelectrons generated at the photocathode are included. It has to be noted that this definition includes the loss due to zero multiplication of a photoelectron at the first dynode. This signal loss is visible as the little peak in the single photoelectron contribution at the position of the pedestal. By definition ℓ_5 dominantly depends on the quality of the fit of the single photoelectron contribution to the signal spectrum. An additional dependency on the fit to the pedestal arises through the usage of the threshold cut defining the borders of the integrals over the single photoelectron contribution. As the pedestal generally is well determined the uncertainty due to the pedestal dependency is neglected. The definition ℓ_3 defines signal loss as all events below the threshold cut which are not accounted for by the pedestal contribution to the spectrum. It therefore accounts for the total loss of all contributions to the signal. In contrast to ℓ_5 the definition of ℓ_3 exclusively depends on the fit of the pedestal part of the signal spectrum.

Figure 27 illustrates the behaviour of the signal loss ℓ_5 found under the various experimental conditions. Figure 28 displays its dependence on the S/N for a representative set of data samples making the general dependence clearly visible. The loss approaches 100 % for small values of S/N and ℓ_5 can drop to $\mathcal{O}(2\,\%)$ for sufficiently large values of S/N.

First the three readout systems shall be compared for the case the "high-gain" option is used. One finds that for the same value of S/N in a measurement with the standard APVm readout the signal loss ℓ_5 is found about 25 % larger than in a measurement with the APVm readout with bypassed attenuation and about 50 % larger than for CAMAC data. At the same time measurements with the CAMAC system can reach up to ~ 5 times larger values of S/N than the standard APVm readout and up to ~ 10 times larger values than the APVm readout with bypassed attenuation. This is caused by the different dynamic ranges of the systems. In effect this means that the lowest value of signal loss was achieved using the CAMAC readout at the highest possible supply voltage (-1000 V). In a different view one finds for a given level of loss smaller values of S/N are sufficient for the APVm system with bypassed attenuation or the CAMAC system than for the standard APVm readout, provided the levels of S/N can be reached within the available dynamic range.

If now a signal loss of the single photoelectron signal of e.g. less than 10 % is required the typical minimum S/N ratios for the "high-gain" options are about 32, 26 and 24 for the standard APVm, the APVm system with bypassed attenuation and the CAMAC system, respectively.

Using lower gain options with any of the readout systems has two effects. The reduction in gain significantly reduces the S/N at a particular supply voltage as the noise level does not change. At the same time the relative width of the single photoelectron contribution to the MaPMT signal spectrum gets smaller. Figure 29 illustrates this effect for one of the data points shown in Figure 28 using the CAMAC readout. Corresponding signal spectra for the two readout systems using the APVm electronics are shown in Figures 30 and 31. This reduces the effect the decreasing S/N has on the signal loss. For the majority of the data points slightly smaller loss figures are found for the lower gain options at comparable S/N ratios. This is interpreted as a result of the increased electron multiplication at the first few dynode stages of the MaPMT causing a reduction in the relative width of the Poissonian signal spectrum. These findings confirm that the gain of the MaPMT can be reduced by changing the resistor ratios of the voltage divider chain without the penalty of an additional loss of signals.

As concluded in Section 6.3 the signal contribution which is parameterised by the so called 'photo-conversion at the first dynode' in the fit probably is caused by two different sources of incompletely sampled signals. Judging from the signal spectra this contribution to the signal spectrum is considerably larger for the APVm data than for the CAMAC data. Such a contamination of the signal obviously may spoil the fit to the signal spectrum. As discussed in [13] the width of the single photoelectron contribution is likely to get widened in the fit the stronger such a contamination becomes. Such a deformation then leads to a stronger overestimate of the signal loss ℓ_5 which has to regarded as an upper limit.

As the CAMAC data is less affected by this problem the signal loss of the single photoelectron contribution, ℓ_5, is expected to be found most reliably in these data sets, cf. Figure 28. As before this interpretation only can be verified using an improved light source. The region between pedestal and single photoelectron peak then should become depopulated and the signal loss will be determined in a more reilable way.

Figure 32 shows the signal loss determined using the definition ℓ_3, i.e. depending only on the fit of the pedestal of the signal spectrum. The data points for all gain options of any individual readout system basically fall on the same curve. For the same S/N the signal loss found in the CAMAC data is smaller

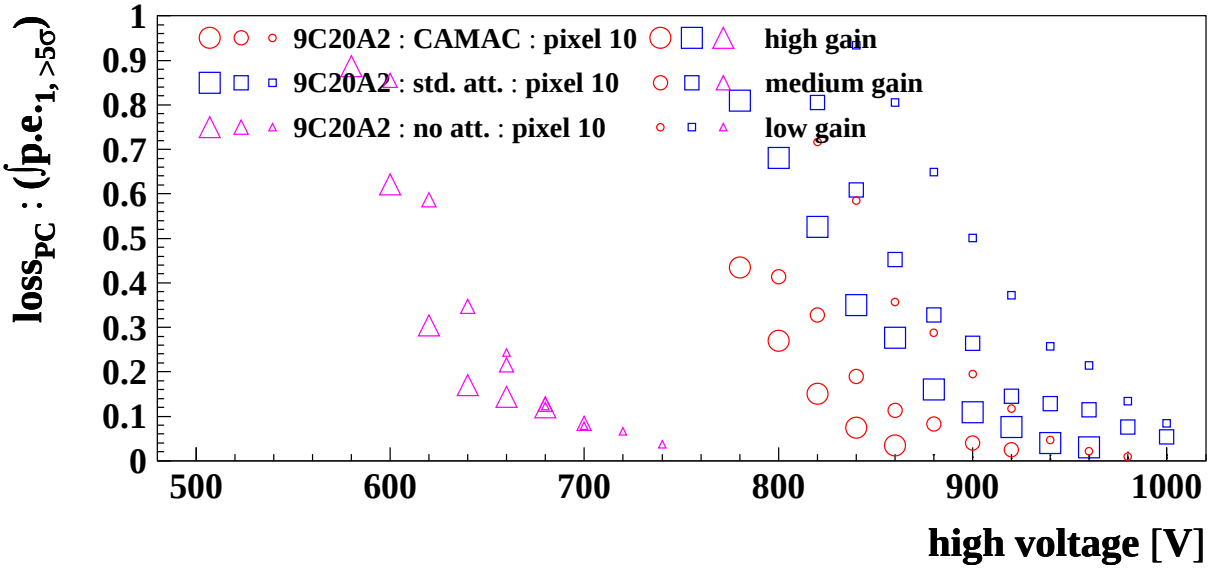

Figure 27: Signal loss, ℓ_5, vs. supply voltage; example data set illustrating the loss behaviour under the various experimental conditions.

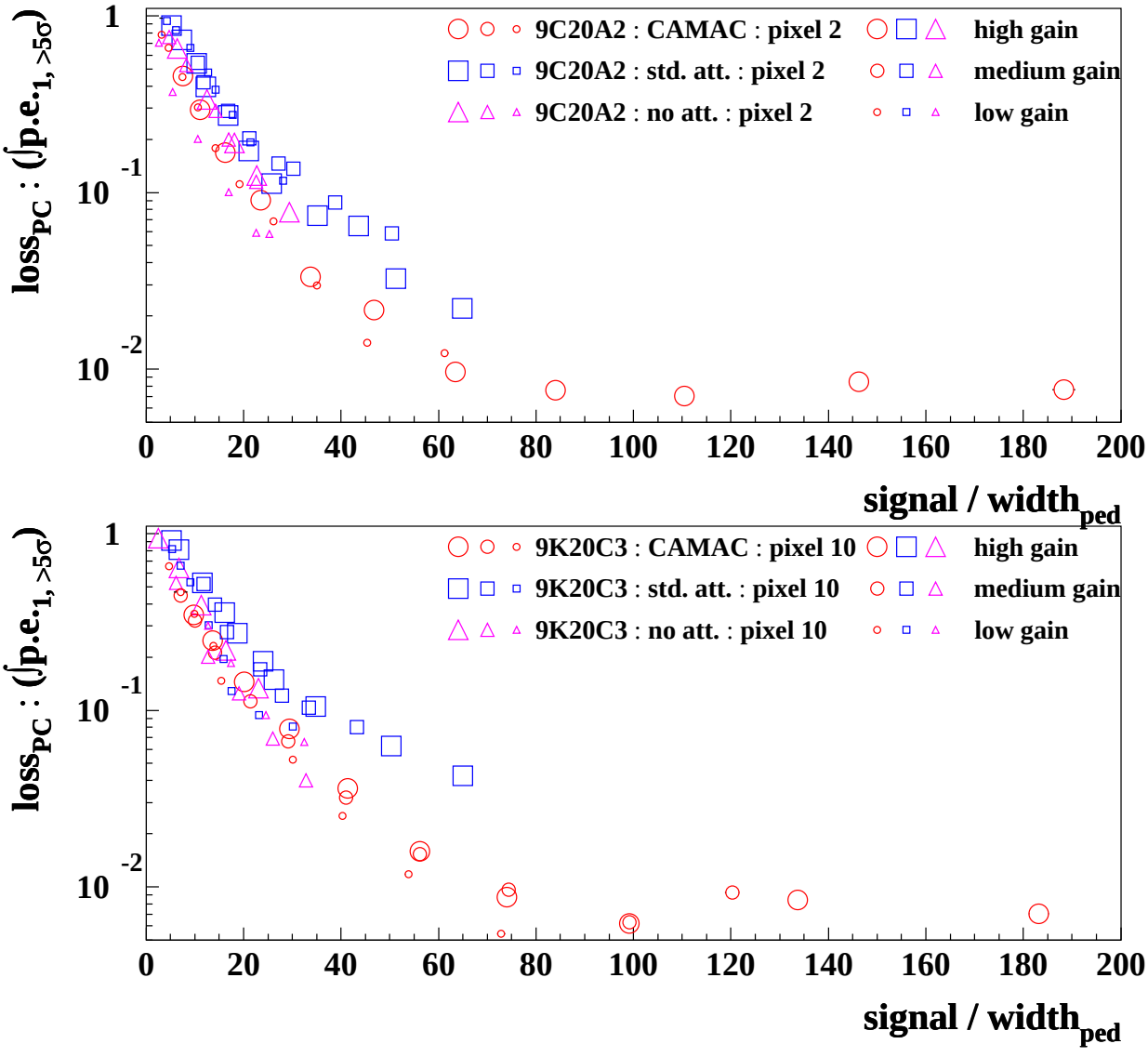

Figure 28: Signal loss, ℓ_5, of MaPMT signal due to a threshold cut $S > Q_0 + 5\sigma_0$ for representative data samples; the definition ℓ_5 depends on the fit of the single photoelectron contribution regarding only photoelectrons (*p.e.*) generated at the photocathode (PC).

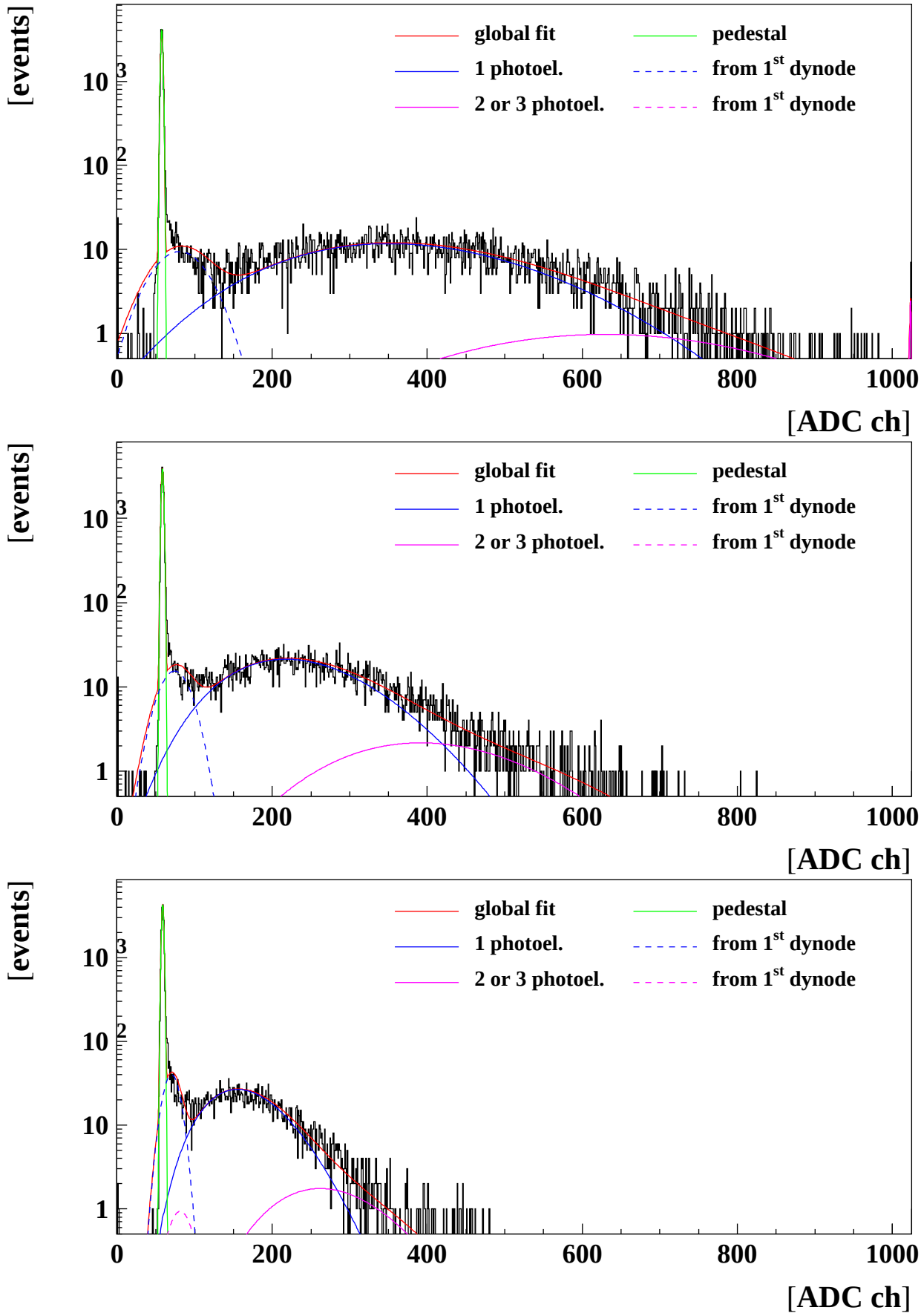

Figure 29: MaPMT signal spectra (tube 9K20C3, pixel 10, -1000 V) using the CAMAC readout and (from top to bottom) the "high-", "medium-" and "low-gain" option.

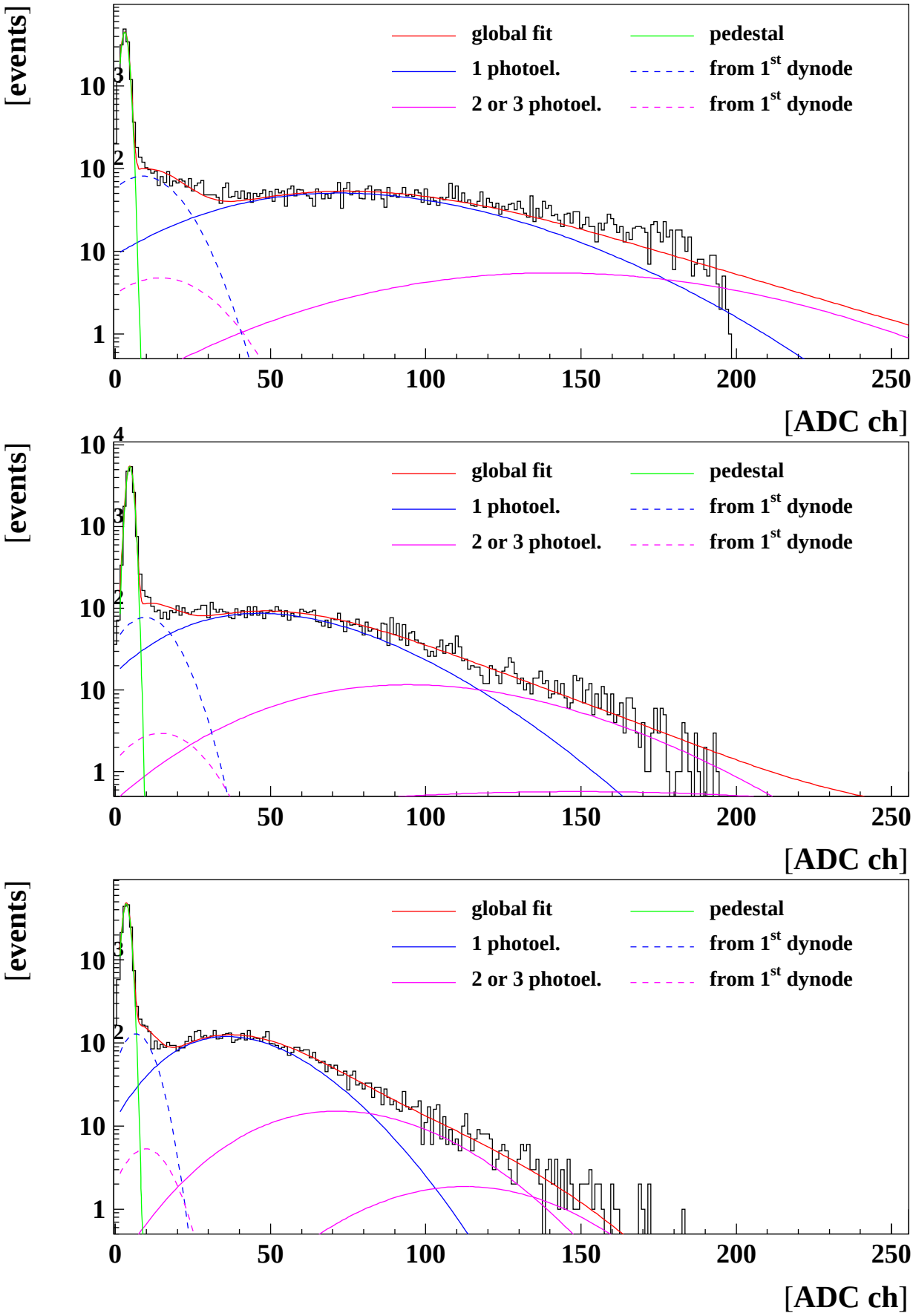

Figure 30: MaPMT signal spectra (tube 9K20C3, pixel 10, -1000 V) using the standard APVm readout and (from top to bottom) the "high-", "medium-" and "low-gain" option.

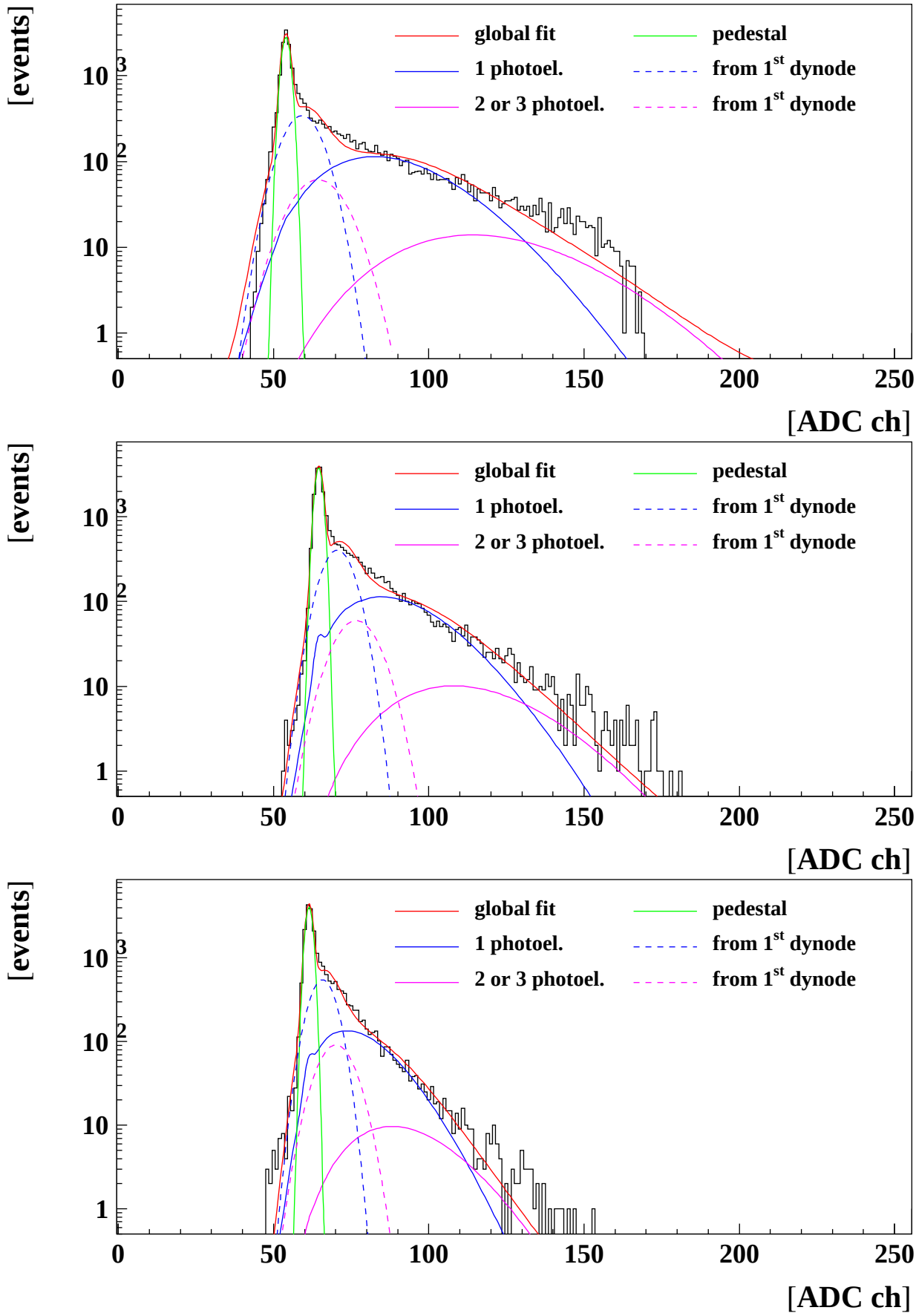

Figure 31: MaPMT signal spectra (tube 9K20C3, pixel 10, -660 V) using the APVm readout with bypassed attenuation and (from top to bottom) the "high-", "medium-" and "low-gain" option.

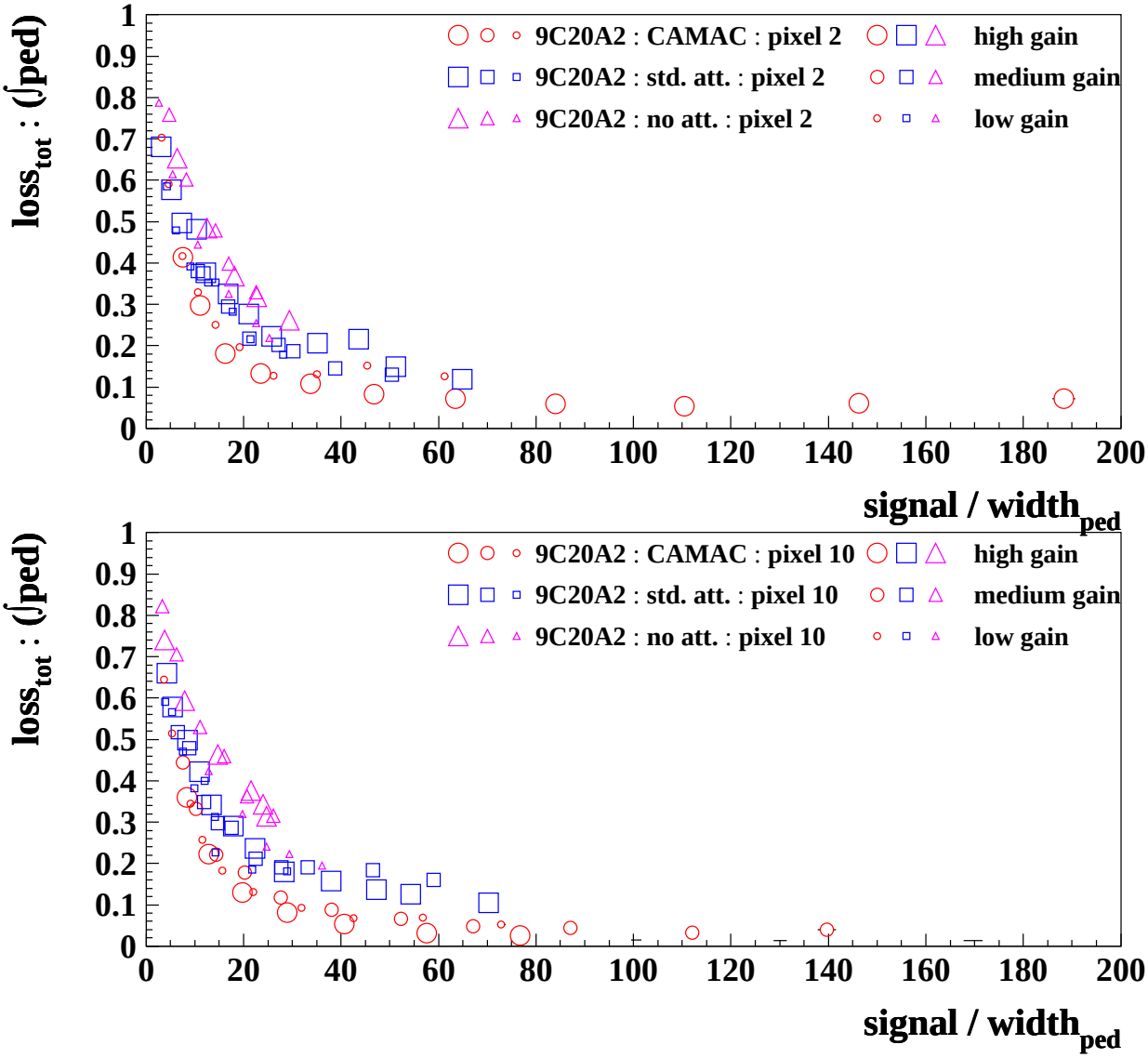

Figure 32: Signal loss, ℓ_3, of MaPMT signal due to a threshold cut $S > Q_0 + 5\sigma_0$ for representative data samples; the noise definition ℓ_3 depends on the fit of the pedestal and accounts for the loss of all contributions to the signal.

by a factor of ~ 2 compared to the standard APVm readout. This can be understood by the smaller contribution of low gain signals in the CAMAC spectra which have a higher fraction of signals below the threshold cut than the single photoelectron contribution to the spectrum. The signal loss found with the APVm system with bypassed attenuation is again about a factor 1.25 larger than found for the standard APVm readout. This is attributed to the even higher level of low gain signals in the spectra there with the subsequently increased loss below the threshold cut. A comparison of the Figures 30 and 31 illustrates that.

For the CAMAC data the lowest achieved loss ℓ_3 is $\mathcal{O}(4\,\%)$, i.e. ~ 5 times larger than for the definition ℓ_5. The loss in the APVm systems seems to level off at $\mathcal{O}(12\,\%)$, i.e. ~ 2.5 times larger than for the definition ℓ_5, but the S/N to achieve that level is barely reached. From Figures 29 to 31 one can see that the loss of the single photoelectron signal as defined in ℓ_5 only is a minor contribution to the loss ℓ_3 for spectra with high gain. As the gain of the tube is decreased the fraction ℓ_5/ℓ_3 grows towards unity. At high gain most of the signal loss ℓ_3 arises from the signal contribution between the pedestal and the single photoelectron peak which is assumed to be caused by incompletely sampled signals. The found behaviour of ℓ_3 in the three data acquisition systems is consistent with that. Also the relative values of ℓ_3 for the CAMAC and the APVm data match the relative amount of the signals in the region between pedestal and single photoelectron peak found. In this interpretation the total loss ℓ_3 dominantly measures at high tube gain the loss due to underestimated signal sizes. And the relative values found for the readout systems

indicate that in the APVm systems about twice as many signals get incompletely sampled than in the CAMAC system.

7 Summary

The approach to reduce the overall signal gain of the MaPMTs by variation of the resistor chain was successful but not completely satisfying for the application in the LHCb RICH detectors. The reduction in gain achieved between the "high-gain" and the "low-gain" option was ≈ 3.5 or only ≈ 2.5, depending on whether the calibration was based on the CAMAC or on the APVm readout, respectively, but there was no means to decide which calibration was correct. Only a reduction in supply voltage or an attenuation of the signal can provide the needed reduction of $\sim \frac{1}{10}$ to match the dynamic ranges of the MaPMT signals and the front-end electronics to be used for the LHCb RICH detectors. At the same time it was shown that a reduction of gain by the modification of the resistor chains could be achieved without the penalty of an additional signal loss due to the reduced S/N ratio as the width of the single photoelectron distribution was reduced as well.

An intercalibration bridging the gap between the APVm readout with the bypassed attenuation and the two other systems was achieved consistent with the hardware parameters. With that and after calibration a description of the signal gain was found consistent for all readout systems and gain options spanning a range of $< 3 \cdot 10^4 \ldots > 5 \cdot 10^6\, e^-$ for the size of the single photoelectron peak. In contrast to the reference data quoted by Hamamatsu an exponential gain behaviour was observed with respect to the supply voltage with a nearly constant slope over the given dynamic range of the signals. Rather the used electronics than the exponential gain behaviour of the MaPMT appear to be the limitation here.

A gain model describing the gain at the individual dynodes of the MaPMT was fitted to the data. It was found that all data sets could be described with a universal parameter, k, which is the exponent to the potential in front of the dynodes. The model underestimated the change in total gain for changes made in the resistor chain if also the normalisation parameter, a, was made universal. Nevertheless the model gives insight to the gain behaviour along the dynodes within a MaPMT. Comparing that with the findings from the data it was concluded that no contribution was found in the signal spectra of any of the used readout systems which would be consistent with a photo-conversion at the first dynode. Instead the additional contribution to the signal spectra between the pedestal and the single photoelectron peak was interpreted as incompletely sampled signals. Due to the different timing used two different sources for incompletely sampled signals must be present for the CAMAC and the APVm type readout. The contamination of the signal spectra with such signals appears to be about twice as strong for the APVm systems as for the CAMAC system. A verification of this interpretation with an improved pulsed light source is pending.

The signal loss has been studied for the used readout systems and gain options and depends in a particular configuration on the S/N ratio achieved. The total signal loss turned out to be dominated by the contribution to the signal spectra between the pedestal and the single photoelectron peak. For the detailed comparison of the data sets the loss of the single photoelectron contribution to the signal spectra was regarded. It was found that at the same S/N the loss of the single photoelectron signal was about 50 % (25 %) times larger for the standard APVm system than for the APVm system with bypassed attenuation (CAMAC system). This converts to a minimum S/N ratio needed to reach a particular loss level which turned out to be about 30 % (10 %) times larger for the standard APVm system than for the APVm system with bypassed attenuation (CAMAC system). The CAMAC system therefore in is the least demanding readout system to reach a particular loss level.

The overall lowest loss figure for the single photoelectron signal was found in the CAMAC data at the highest supply voltage as its wide dynamic range allowed for very high values of S/N. The lowest loss figures reachable with the APVm readout with bypassed attenuation generally were signifficantly higher than for the other two systems. This is due to the particular limitations in the dynamic range of the APVm readout with bypassed attenuation. So unless a configuration can be found which allows for a larger dynamic range the direct input of MaPMT signals into front-end chips designed to read out silicon detectors is to be disfavoured due to the unsatisfactory loss levels achieved. The safest option for the readout of the LHCb RICH detectors rather is an adaptation of the dynamic ranges by an attenuation of the MaPMT signals before the sampling in the front-end. An implementation of the attenuation circuit into the front-end of the finally chosen readout chip clearly is preferred to a passive attenuation circuit in front of the chip as used in this study. This will avoid the massive cross-talk problems experienced with the passive attenuation circuit discussed in [5]. Several schemes of attenuation are possible. Manpower has to be invested to design, implement and evaluate the several possible schemes of attenuation into the

front-end chip of choice, e.g. the Beetle chip.

This in mind it would be sensible to adapt the dynamic range of the input circuit to the gain obtained when the tubes are operated with the default parameters recommended by Hamamatsu. In the case the interpretation concerning the incompletely sampled signals turns out to be correct such a system should exhibit a loss characteristic as discussed for the CAMAC data. A slightly lower loss of the single photoelectron signal then could be achieved by applying the "low-gain" option for the resistor chain and simultaneously increasing the supply voltage by 50...100 V to again make use of the same dynamic range of the system as without these alterations.

8 Conclusion

The readout of Multianode Photomultiplier Tubes has been studied using three different readout systems: one based on CAMAC electronics and two based on the APVm readout chip originally developed to readout silicon detectors. In one instance the dynamic range of the MaPMT signals was matched to the APVm input by an AC-coupling attenuation network in front of the APVm chip. In the second instance the attenuation circuit was bypassed and the signal size of the MaPMT basically was adjusted to the APVm input circuit by reducing the supply voltage to the tube. For all three systems three options of the resistor chain were used to distribute the supply voltage to the dynodes of the tubes. The options with reduced overall signal gain were designed to also reduce the width of the single photoelectron distribution in the signal spectrum by increasing the electron multiplication at the first (few) dynodes of the tube.

The gain of the single photoelectron peak and the loss of the single photoelectron signal was studied. A consistent description of the gain was found for all readout systems and gain options for signal sizes spanning a range of $< 3 \cdot 10^4 \ldots > 5 \cdot 10^6\, e^-$. The studied readout systems were evaluated regarding the loss of single photoelectron signal in the dynamic range available. For the use in the LHCb RICH detectors it was recommended to facilitate a matching of the dynamic range of the MaPMT signals to the final readout chip by the incorporation of an application specific attenuation circuit into front-end of the chip itself.

We thank Steve Wotton for the support in the setup of the APVm readout system and Becki Cikoski for her work on the development on the used fitting algorithm.

References

[1] "A Large Hadron Collider Beauty Experiment for Precision Measurements of CP Violation and Rare Decays"; LHCb Technical Proposal, LHCC 98/04, LHCC/P4 (Feb. 1998).

[2] S. Amato et al., "LHCb - RICH Technical Design Report", CERN/LHCC/2000-0037, LHCb TDR 3, Sep 2000.

[3] The LHCb RICH detector web page: "http://lhcb.cern.ch/rich/".

[4] F. Muheim et. al., "Proposal for Multi-Anode Photo Multiplier Tubes as photo detectors for the LHCb RICH", LHCb 2000-065 RICH.

[5] E. Albrecht et. al., "Performance of a cluster of multi-anode photomultipliers equipped with lenses for use in a prototype RICH detector", Nucl. Inst. Meth. **A 488** (2002) 110; LHCb 2000-083 RICH, LHCb 2001-091 RICH.

[6] A. Duane et. al., "Čerenkov Rings Detected with Multinaode P.M.T", LHCb 1998-039 RICH.

[7] N. Smale et. al., "Evaluation of the Multianode Photomultiplier for the LHCb RICH detectors", LHCb 1998-066 RICH.

[8] E. Albrecht et. al., "Latest beam test results from RICH prototypes using hybrid photo detectors and multi anode PMTs", Nucl. Inst. Meth. **A 433** (1999) 159

[9] E. Albrecht et. al., "A prototype RICH detector Using Multi-Anode Photo Multiplier Tubes and Hybrid Photo-Diodes", Nucl. Inst. Meth. **A 456** (2001) 233; LHCb 2000-068a/b RICH.

[10] The LHCb-Beetle web page: "http://wwwasic.kip.uni-heidelberg.de/ lhcb/".

[11] M.D.M. de Fez-Laxo et. al., Nucl. Inst. Meth. **A 382** (1996) 533
M. Raymond et. al., "Electronics for the LHC Experiments", CERN/LHCC/97-60 (1997) 158
L.L. Jones et. al., "Electronics for the LHC Experiments", CERN/LHCC/98-36 (1998) 185.

[12] S. Eisenhardt et. al., "Study of Multi Anode Photo Multiplier Tubes at Low Gains", LHCb 2000-088 RICH.

[13] S. Eisenhardt et. al., "Analysis of signal spectra of Multianode Photo Multiplier tubes", LHCb 2004-016 RICH.

[14] Hamamatsu, private communications.

[15] S.A. Baird et. al., "Electronics for the LHC Experiments", Snowmass 1999, CERN/LHCC/98-33 (1999) 357.

[16] J. Coughlan, "CMS Front-End Driver PMC User Manual", Rutherford Appleton Laboratory, unpublished.

[17] M. French, "APV6 User Manual", Rutherford Appleton Laboratory, unpublished.